JGR Atmospheres

RESEARCH ARTICLE
10.1029/2022JD038052

Special Section:
The Arctic: An AGU Joint Special Collection

Exceptional Wildfire Enhancements of PAN, C_2H_4, CH_3OH, and HCOOH Over the Canadian High Arctic During August 2017

T. Wizenberg[1], K. Strong[1], D. B. A. Jones[1], E. Lutsch[1], E. Mahieu[2], B. Franco[3], and L. Clarisse[3]

[1]Department of Physics, University of Toronto, Toronto, ON, Canada, [2]Institute of Astrophysics and Geophysics, UR SPHERES, Université de Liège, Liège, Belgium, [3]Service de Chimie Quantique et Photophysique, Atmospheric Spectroscopy, Université Libre de Bruxelles (ULB), Brussels, Belgium

Key Points:

- The 2017 Canadian wildfires produced the largest PAN, C_2H_4, and HCOOH column enhancements observed in the high Arctic from 2006 to 2020
- GEOS-Chem effectively simulates the observed plume transport, but required modifications to the injection heights of the fire emissions
- Mid-latitude wildfires may become an increasingly significant source of reactive VOC species to the high Arctic during the summer months

Supporting Information:

Supporting Information may be found in the online version of this article.

Correspondence to:

T. Wizenberg,
wizenberg@atmosp.physics.utoronto.ca

Citation:

Wizenberg, T., Strong, K., Jones, D. B. A., Lutsch, E., Mahieu, E., Franco, B., & Clarisse, L. (2023). Exceptional wildfire enhancements of PAN, C_2H_4, CH_3OH, and HCOOH over the Canadian high Arctic during August 2017. *Journal of Geophysical Research: Atmospheres*, *128*, e2022JD038052. https://doi.org/10.1029/2022JD038052

Received 21 OCT 2022
Accepted 2 MAY 2023

Abstract Extreme enhancements in the total columns of carbon monoxide (CO), peroxyacetyl nitrate (PAN), ethylene (C_2H_4), methanol (CH_3OH), and formic acid (HCOOH) were observed over the Canadian high Arctic during the period of 17–22 August 2017 by a ground-based Fourier transform infrared (FTIR) spectrometer at Eureka, Nunavut (80.05°N, 86.42°W), and by the Infrared Atmospheric Sounding Interferometer (IASI) satellite instruments. These enhancements have been attributed to wildfires in British Columbia (BC) and the Northwest Territories (NWT) of Canada, and represent the largest short-term perturbations of PAN, C_2H_4, and HCOOH above ambient concentrations over the 14-year (2006–2020) Eureka time-series. Enhancement ratios, emission ratios, and emission factors relative to CO were calculated for all species for both FTIR and IASI observations. The C_2H_4 and HCOOH emission factors are significantly larger than previous studies, suggesting unusually high emissions from these fires. The wildfire plumes were also simulated using the GEOS-Chem model. Initial GEOS-Chem simulations displayed a severe under-estimation relative to observations for these fire plumes resulting from the injection height scheme of the model. Sensitivity tests highlighted that injection heights of 12.5 km for BC (based on previous studies) and 10 km for the NWT fires yielded the strongest correlations with ground-based measurements. Applying these injection heights to the model significantly improves the simulated plume transport and agreement with ground- and space-based observations. GEOS-Chem was also used to estimate the magnitude of secondary in-plume production of CH_3OH and HCOOH; it was found to be an important component (∼18%) of the enhanced HCOOH columns at Eureka.

Plain Language Summary Wildfires are a significant natural source of pollution to the atmosphere. During mid-August 2017, two extremely large wildfires occurred simultaneously in British Columbia (BC) and the Northwest Territories (NWT) of Canada. These fires produced an exceptional amount of smoke, which was subsequently transported to the Canadian high Arctic region. The atmospheric concentrations of carbon monoxide (CO), peroxyacetyl nitrate (PAN), ethylene (C_2H_4), methanol (CH_3OH), and formic acid (HCOOH) contained within these transported smoke plumes were measured using both a ground-based infrared spectrometer located at Eureka, Nunavut (80.05°N, 86.42°W) and satellite instruments. The largest concentrations of CO, PAN, C_2H_4, and HCOOH observed over the 14-year measurement record (2006–2020) of the ground-based spectrometer were due to these wildfires. The emissions of these fires were estimated from both the ground- and space-based measurements and were found to be unusually high in comparison to previous studies. The wildfire smoke plumes were also simulated using a chemical transport model, but the model was found to inject the smoke too low into the atmosphere above the fires; after adjustments to the injection scheme were made, the agreement of the model with the measurements was significantly improved.

1. Introduction

Volatile organic compounds (VOCs) represent a large family of highly reactive and typically short-lived trace gases that reside in the Earth's atmosphere. VOCs have a broad range of primary and/or secondary sources, including anthropogenic emissions, biogenic production, and biomass burning. These reactive species can have wide-reaching direct and indirect effects on the air quality and climate of remote regions. In the Arctic, local sources of VOCs are limited, and their short atmospheric lifetimes generally hinder large-scale transport from sources at lower latitudes. However, biomass burning and the subsequent injection of smoke plumes into the upper troposphere—lower stratosphere (UTLS), coupled with increased competition for reactants within these

plumes, can extend chemical lifetimes and allow significant short-term perturbations in the VOC budgets of the high-Arctic region.

In this paper, we focus on four biomass burning-linked reactive trace gases in particular; peroxyacetyl nitrate (PAN), ethylene (C_2H_4), methanol (CH_3OH), and formic acid (HCOOH). PAN is the largest thermally unstable reservoir of nitrogen oxide radicals (NO_x), with a lifetime ranging from 1 hr at 298 K to several months at the colder temperatures found in the UTLS (Bridier et al., 1991; D. Jacob, 2000; Orlando et al., 1992; Talukdar et al., 1995; Tuazon et al., 1991). This property of PAN enables its long-range transport from polluted source regions to remote regions such as the Arctic, where it influences tropospheric O_3 production and contributes to the seasonal pollution phenomenon known as "Arctic haze" (Fischer et al., 2011, 2014; Kasibhatla et al., 1993; Law et al., 2014; Law & Stohl, 2007; Moxim et al., 1996; Wang et al., 1998). PAN is not directly emitted in biomass burning, but rather it is formed rapidly via secondary production within biomass burning plumes, which typically contain high concentrations of PAN precursors including NO_x, and non-methane volatile organic compounds (NMVOCs) such as acetone (C_3H_6O) and acetaldehyde (CH_3CHO) (Akagi et al., 2011; Alvarado et al., 2010; Juncosa Calahorrano et al., 2020, 2021; Liu et al., 2016; Yokelson et al., 2009).

C_2H_4 is one of the most abundant atmospheric unsaturated hydrocarbons, with emissions estimated at around 20 Tg/year, approximately half of which is from biomass burning (Folberth et al., 2006; Herbin et al., 2009; Horowitz et al., 2003). C_2H_4 is only directly emitted, and there are currently no known atmospheric production pathways (Folberth et al., 2006; Sawada & Totsuka, 1986). C_2H_4 has a short atmospheric lifetime of approximately 1 to 3 days due to its reactivity with the hydroxyl radical (OH) and ozone (O_3), which yields small amounts of several important trace gases and minor atmospheric constituents including carbon monoxide (CO), carbon dioxide (CO_2), and formaldehyde (HCHO), as well as HCHO and O_3 precursors (Alvarado et al., 2011; Dolan et al., 2016; Olivella & Solé, 2004; Sawada & Totsuka, 1986; Toon et al., 2018).

CH_3OH is the most abundant NMVOC in the Earth's atmosphere, with a lifetime on the order of 6 days in the troposphere (Stavrakou et al., 2011). CH_3OH affects the oxidative capacity of the atmosphere through its primary atmospheric sink via photochemical oxidation by OH, and it contributes to the production of CO, HCHO, and tropospheric O_3 (Millet et al., 2008; Singh et al., 2001; Stavrakou et al., 2011; Tie et al., 2003; Wells et al., 2014).

HCOOH is most abundant atmospheric carboxylic acid in the troposphere, with a lifetime of approximately 4 days (Stavrakou et al., 2012). Primary sources of HCOOH include anthropogenic emissions, direct emissions from plant leaves, and biomass burning; meanwhile it is removed from the atmosphere via its reaction with OH, and through dry and wet deposition. HCOOH can significantly influence atmospheric acidity, particularly in remote regions such as the Arctic (Chameides & Davis, 1983; Galloway et al., 1982; Franco et al., 2021; D. J. Jacob, 1986; Keene et al., 2015; Millet et al., 2015; Stavrakou et al., 2012; S. Yu, 2000).

Due to the scarcity of reliable long-term measurements in the Arctic region, the budgets of PAN, C_2H_4, CH_3OH, and HCOOH, including the relative contributions of biomass burning, are currently not well constrained. For studies of reactive species such as these at high latitudes, the use of a ground-based Fourier transform infrared (FTIR) spectrometer is advantageous because these instruments generally possess greater vertical sensitivity, and lower detection limits than nadir-viewing satellite instruments, particularly in the Arctic where low thermal contrast presents challenges for space-based infrared measurements. Additionally, the use of a ground-based FTIR enables the simultaneous measurements of many species, and can provide a long-term time series of each measured trace gas. In the Canadian high Arctic, ground-based FTIR measurements made at Eureka, Nunavut (80.05°N, 86.42°W) have previously been used to investigate transported boreal wildfire pollution, as shown by Lutsch et al. (2016, 2019) and Viatte et al. (2013, 2014, 2015). Simultaneous ground-based FTIR retrievals of C_2H_4, CH_3OH, and HCOOH were first described in Paton-Walsh et al. (2005, 2008), and have been applied to a broad range of biomass burning studies (e.g., Paton-Walsh et al., 2005, 2008; Paulot et al., 2011; Viatte et al., 2014, 2015; Vigouroux et al., 2012). Ground-based FTIR retrievals of PAN, however, are extremely novel and were first demonstrated by Mahieu et al. (2021). To our knowledge, this is the first study to apply these new retrievals of PAN to investigate biomass burning emissions.

Ground-based measurements can be complemented by satellite observations where available, and concentrations of PAN, C_2H_4, CH_3OH, and HCOOH have been retrieved from several satellite instruments including the Atmospheric Chemistry Experiment Fourier Transform Spectrometer (ACE-FTS; Coheur et al., 2007; Dufour et al., 2006; González Abad et al., 2009; Tereszchuk et al., 2013), the Tropospheric Emission Spectrometer

(TES; Cady-Pereira et al., 2012, 2014; Dolan et al., 2016; Payne et al., 2014), the Infrared Atmospheric Sounding Interferometer (IASI; Coheur et al., 2009; Pommier et al., 2016; Razavi et al., 2011), and the Cross-track Infrared Sounder (CrIS; Payne et al., 2022). Due to low ambient concentrations, high cloud cover, and the aforementioned issue of poor thermal contrast, difficulties are often encountered when attempting to retrieve these reactive species from satellite measurements in the polar regions. Recently, artificial neural network retrievals for IASI (ANNI) of PAN, HCOOH, CH_3OH, and C_2H_4 have been developed (Franco et al., 2018, 2022). These ANNI retrievals provide improved sensitivity over classical optimal estimation method (OEM) retrievals, potentially enhancing our ability to observe these VOCs over high-latitude regions (Franco et al., 2018). ANNI products have already been used in biomass burning studies of NH_3 (Whitburn et al., 2015, 2016, 2017), HCOOH and acetic acid (CH_3COOH) (Franco et al., 2020), and most recently HCN (Rosanka et al., 2021).

In addition to ground- and space-based observations of VOCs, global chemical transport models (CTMs) such as GEOS-Chem (Bey et al., 2001) can provide another valuable perspective on the transport and chemistry of biomass burning plumes, filling in gaps where there are sparse or no measurements available. Simulations of PAN, CH_3OH, HCOOH, and C_2H_4 are included in the current version of the model (C_2H_4 was recently added in version 13.3.0 in November 2021). The GEOS-Chem model has been used to study the influence of wildfires (e.g., Alvarado et al., 2010; Chen et al., 2021; Lutsch et al., 2019; Paulot et al., 2011). Previous studies have shown that chemical transport models, including GEOS-Chem, consistently underestimate HCOOH and CH_3OH mixing ratios relative to observations, with the largest biases occurring at high latitudes, possibly indicating unknown local sources, missing chemistry, or inaccurate emissions (Bates et al., 2021; Chen et al., 2019; Franco et al., 2021; Millet et al., 2015; Paulot et al., 2011; Schobesberger et al., 2016; Stavrakou et al., 2012). As a result, it is important to routinely evaluate model performance against observations, particularly for lesser-studied atmospheric constituents.

In this study, we use a combination of ground-based FTIR measurements from Eureka, IASI satellite observations, and global simulations from the GEOS-Chem CTM to investigate the influence of two independent fires which occurred in British Columbia (BC) and the Northwest Territories (NWT) of Canada during August 2017. The BC wildfires were exacerbated by persistent warm and dry conditions brought on by climate change, and affected a record 1.2×10^6 ha while displacing approximately 65,000 people (BC Wildfire Service, 2017; Kirchmeier-Young et al., 2019). These fires resulted in a volcano-like stratospheric smoke plume that encircled the tropical and extra-tropical northern hemisphere and lingered for several months (Fromm et al., 2021; Khaykin et al., 2018; Kloss et al., 2019; Peterson et al., 2018). Due to the far-reaching effects of anthropogenic climate change, wildfires are predicted to continue to increase in frequency and severity (Flannigan et al., 2005; Halofsky et al., 2020; Hope et al., 2016), and extreme pyrocumulonimbus (pyroCb) events are expected to become more commonplace (Peterson et al., 2021). As a result, the 2017 wildfires may serve as a bellwether for future biomass burning events, and may forecast a substantial increase in wildfire-related VOC concentrations in the high Arctic, which has significant implications for the sensitive climate and environment of the region.

This paper is structured as follows. The ground-based FTIR instrument and retrievals, the IASI satellite observations, and the GEOS-Chem model used in this study are described in Section 2. The observed enhancements from the ground-based FTIR at Eureka and IASI are presented in Section 3.1. The trace-gas correlations and emission estimates calculated from fire-affected ground-based and IASI observations at Eureka are presented and discussed in relation to previous studies in Section 3.2. In Section 3.3 we compare the GEOS-Chem CTM to the ground-based FTIR and IASI observations, discuss the implications of the biomass burning emissions injection scheme on the simulated plume transport, and estimate the effect of secondary in-plume production on the total columns of C_2H_4, CH_3OH, and HCOOH at Eureka. Conclusions are presented in Section 4.

2. Methods

2.1. The PEARL-FTIR

The ground-based instrument used in this study is a Bruker IFS 125HR FTIR spectrometer located at the Polar Environment Atmospheric Research Laboratory (PEARL) at Eureka, Nunavut (80.05°N, 86.42°W, 610 m a.s.l) in the Canadian high Arctic. The instrument was installed at PEARL in July 2006, and measurements are made during sunlit clear-sky conditions using a custom-built solar tracker. Trace gas profiles and total column concentrations are retrieved from the measured solar-absorption spectra, and are regularly contributed to the Network for

the Detection of Atmospheric Composition Change (NDACC; www.ndacc.org). Measurements are made in the mid-infrared at a spectral resolution of 0.0035 cm^{-1} using a potassium bromide (KBr) beam splitter that covers the spectral range of 700–5000 cm^{-1}, a series of optical filters, and two detectors; a photovoltaic indium antimonide (InSb) detector (1850–10,000 cm^{-1}), and a mercury cadmium telluride (HgCdTe) detector (600–6000 cm^{-1}). At present, the time-series of PEARL-FTIR measurements extends from August 2006 until March 2020, when the COVID-19 pandemic halted nominal operations. A detailed description of the PEARL-FTIR is provided in Batchelor et al. (2009).

2.2. FTIR Retrieval Methods

The measured high-resolution solar-absorption spectra are processed using the SFIT4 retrieval algorithm version 0.9.4.4 (https://wiki.ucar.edu/display/sfit4/) that is based upon the Optimal Estimation Method (Rodgers, 2000), and which iteratively adjusts the trace gas volume mixing ratio profile until the difference between the calculated and measured spectra is minimized. The forward model of SFIT4 is a line-by-line radiative transfer model that encompasses multiple atmospheric layers (47 in the case of Eureka), and which assumes a Voigt line shape function (Notholt et al., 2006). For the retrievals of CO, CH_3OH, and HCOOH spectroscopic parameters are from the HITRAN 2008 line list database (Rothman et al., 2009). For the retrieval of PAN, H_2O lines from HITRAN 2016 (Gordon et al., 2017) were used based on the recommendations of Mahieu et al. (2021), while the spectroscopic parameters of all other species were sourced from HITRAN 2008. For the retrieval of C_2H_4, the updated ATM20 line list was used (Toon, 2022). In the case of any unresolved interfering features, namely those of carbon tetrachloride (CCl_4), chlorine nitrate ($ClONO_2$), CFC-12 (CCl_2F_2), HCFC-22 ($CHClF_2$), HFC-23 (CHF_3), and CFC-113 (CCl_2FCClF_2), we supplement the spectroscopic databases with pseudo-linelists generated by G. C. Toon (Jet Propulsion Laboratory, California Institute of Technology, Pasadena, CA; available from https://mark4sun.jpl.nasa.gov/pseudo.html). Additionally, atmospheric temperature and pressure profiles are provided by the National Centers for Environmental Prediction (NCEP), and the a priori profiles of each species are taken from a 40-year average (1980–2020) of the Whole Atmosphere Community Climate Model (WACCM) version 4 (Marsh et al., 2013).

The spectral fitting microwindows, the interfering species, and corresponding references for each of the PEARL-FTIR retrievals are summarized in Table 1. CO is a standard NDACC product, and is retrieved from PEARL-FTIR measurements following NDACC Infrared Working Group (IRWG) recommendations and the harmonized microwindows provided by Lutsch et al. (2016), Viatte et al. (2014), and references therein. PAN, C_2H_4, CH_3OH, HCOOH are non-standard products but are retrieved and processed in a similar manner. Three microwindows are used to retrieve CO: a strong line at 2157.50–2159.15 cm^{-1}, and two weak lines 2057.70–2058.00 cm^{-1}, and 2069.56–2069.76 cm^{-1} (Notholt et al., 2000; Viatte et al., 2014; Zhao et al., 2002). For CH_3OH, two windows were used: 992.00–998.70 cm^{-1} and 1029.00–1037.00 cm^{-1} (Bader et al., 2014; Viatte et al., 2014; Vigouroux et al., 2012). For the retrieval of HCOOH, two windows were also used: a primary window spanning 1102.00–1109.00 cm^{-1} that encompasses the ν_6 Q-branch absorption feature, and a small secondary window at 1178.40–1178.80 cm^{-1} to improve the fitting of the interfering species HDO, N_2O, CH_4, and O_3 (Paton-Walsh et al., 2005; Vigouroux et al., 2012; Yamanouchi et al., 2020; Zander et al., 2010). The ground-based FTIR retrieval of PAN is novel and was first described by Mahieu et al. (2021). Here, only a single broad window was used for PAN: 779.90–811.37 cm^{-1} (Mahieu et al., 2021). As discussed in Mahieu et al. (2021), the second PAN retrieval window spanning 1150.57–1178.83 cm^{-1} yielded inconsistent and often unphysical retrieved columns at the polar sites, and a lower signal-to-noise ratio on average. Lastly, C_2H_4 has previously been retrieved from ground-based FTIR instruments using the older SFIT2 algorithm (e.g., Paton-Walsh et al., 2005; Rinsland et al., 2005), but to our knowledge we are the first to implement these retrievals in SFIT4 and present a long-term time-series of C_2H_4 total columns at an Arctic FTIR site. For the retrievals of C_2H_4, we use a single spectral window at 948.80–952.40 cm^{-1} which encompasses the Q-branch absorption feature of the ν_7 band centered around 949 cm^{-1} (Paton-Walsh et al., 2005; Rinsland et al., 2005; Toon et al., 2018).

A full error analysis is performed for all retrievals following the approach of Rodgers (2000). The error budget includes forward model parameter errors, spectroscopic uncertainties and measurement noise error. The mean random, systematic, and total uncertainties, and the average degrees of freedom for signal (DOFS) are tabulated in Table 2. Adding the total random and systematic error components in quadrature gives mean retrieval uncertainties for the total columns of CO, PAN, C_2H_4, CH_3OH, and HCOOH of 2.8%, 25.6%, 67.3%, 11.8%, and 13.2%.

Table 1
Spectral Fitting Microwindows and the Interfering Species Used for the Eureka Fourier Transform Infrared Retrievals and Corresponding References

Target species	Microwindows (cm^{-1})	Interfering species	Reference
CO	2057.70–2058.00,	CO_2, H_2O,	Notholt et al. (2000),
	2069.56–2069.76,	N_2O, O_3,	Zhao et al. (2002),
	2157.50–2159.15	OCS	Viatte et al. (2014)
PAN	779.90–811.37	CO_2, CCl_4,	Mahieu et al. (2021)
		CHF_2Cl, $ClONO_2$,	
		CFC-113, H_2O,	
		O_3	
C_2H_4	948.80–952.40	CO_2, COF_2,	Paton-Walsh et al. (2005),
		H_2O, N_2O,	Rinsland et al. (2005),
		NH_3, O_3,	Toon et al. (2018),
		SF_6	Vander Auwera et al. (2014)
CH_3OH	992.00–998.70,	CO_2, H_2O,	Vigouroux et al. (2012),
		O_3, O_3^{686},	Viatte et al. (2014),
	1029.00–1037.00	O_3^{676}, O_3^{668},	Bader et al. (2014)
		O_3^{667}	
HCOOH	1102.00–1109.00,	CCl_2F_2, CH_4	Zander et al. (2010),
		CHF_2Cl, H_2O,	Vigouroux et al. (2012),
	1178.40–1178.80	HDO, N_2O,	Yamanouchi et al. (2020)
		NH_3, O_3	

The relative uncertainty associated with the C_2H_4 total columns appears very large, however this is primarily due to the extremely low ambient concentrations of C_2H_4 in the Arctic in the absence of biomass burning pollution. During the 17–23 August 2017 fire period, the mean relative uncertainty in the retrieved C_2H_4 columns was 7.9%. The DOFS for CO, PAN, C_2H_4, CH_3OH, and HCOOH are 2.17, 1.02, 1.01, 1.04, and 1.12, respectively. For the retrievals of CO and CH_3OH, we use an empirically tuned a priori covariance matrix to constrain the retrieved profiles, while in the case of the retrievals of PAN, C_2H_4, and HCOOH, Tikhonov regularization was employed (Tikhonov, 1963). A plot of the mean averaging kernel and corresponding retrieval sensitivity calculated over the 2006–2020 time-series for each species is provided as Figure S1 in Supporting Information S1. A sensitivity of 1 indicates that a retrieval is independent of the a priori, while a sensitivity of 0 indicates that the a priori is the retrieved state. CO retrieval has broad sensitivity in the troposphere and stratosphere, with a sensitivity greater than 0.5 between 0 and 55 km. The PAN, C_2H_4, and CH_3OH retrievals are primarily sensitive to the troposphere and lower stratosphere, with sensitivities greater that 0.5 in the range of 0–12 km for PAN and C_2H_4, and 0–13 km for CH_3OH species. The HCOOH retrieval displays slightly broader sensitivity to the lower to mid stratosphere in comparison to PAN, C_2H_4, and CH_3OH, with a sensitivity greater than 0.5 between 0 and 21 km. In general, the retrievals of CO, PAN, C_2H_4, CH_3OH, and HCOOH display good sensitivity to the troposphere and lower stratosphere where biomass burning plumes are likely to be located.

Table 2
Mean Total Column Retrieval Uncertainties and Degrees of Freedom for Signal (DOFS) of the Eureka Fourier Transform Infrared Retrievals Calculated Over the Period of 2006–2020

Species	Random uncertainty (%)	Systematic uncertainty (%)	Total uncertainty (%)	Mean DOFS
CO	1.6	2.3	2.8	2.17
PAN	22.4	8.0	25.6	1.02
C_2H_4	64.0	17.9	67.3	1.01
CH_3OH	4.7	10.5	11.8	1.04
HCOOH	5.3	11.3	13.2	1.12

2.3. IASI Observations

Measurements of CO, PAN, C_2H_4, CH_3OH, and HCOOH retrieved from the IASI-A and IASI-B instruments aboard the MetOp-A and MetOp-B satellites, respectively, were used. The MetOp platforms provide twice-daily global coverage (~9:30 morning and evening), with a swath width of approximately 2200 km, and with a circular footprint of ~12 km in diameter at nadir

(Clerbaux et al., 2009). These properties provide an advantage over other nadir-sounding satellite instruments that can retrieve VOCs such as TES due to denser sampling and global coverage. To maximize the available data and the likelihood of coincident measurements with the PEARL-FTIR, observations from both the A.M. and P.M. overpasses were used in the analysis. IASI data has been extensively used to investigate the emissions and enhancement ratios of reactive VOC species and NH_3 within fire plumes around the world (Coheur et al., 2009; Franco et al., 2020; Paulot et al., 2017; Pommier et al., 2017; R'Honi et al., 2013; Rosanka et al., 2021; Whitburn et al., 2015, 2016, 2017).

Total column concentrations of CO are retrieved using the Fast Optimal retrievals on Layers for IASI (FORLI) algorithm, which is based upon the optimal estimation method (George et al., 2015; Hurtmans et al., 2012). The IASI CO product has previously been validated against ground-based FTIR measurements from the NDACC network by Kerzenmacher et al. (2012), who found no notable biases in the collocated measurements. The vertical abundances of PAN, C_2H_4, CH_3OH, and HCOOH are obtained using the Artificial Neural Network for IASI (ANNI) retrieval algorithm Version 3 (Franco et al., 2018). The HCOOH ANNI product was validated against ground-based NDACC instruments (including the PEARL-FTIR) in Franco et al. (2020), and was found to have generally good agreement (i.e., correlation coefficients greater than 0.6) at most FTIR sites, but a positive bias at high latitudes. The PAN ANNI product was compared against ground-based FTIR measurements at the Jungfraujoch station in Switzerland by Mahieu et al. (2021), who found good agreement (correlation coefficient of 0.77) with no significant bias for the altitude-corrected IASI observations. The PAN ANNI product was also qualitatively compared against the PEARL-FTIR PAN retrieval by Mahieu et al. (2021), however, due to the poor observational conditions for IASI in the absence of strong enhancements (i.e., low thermal contrast), observations were only made during a few summer months, and a general high bias relative to the ground-based measurements was seen. The C_2H_4 ANNI retrieval is new and is described in Franco et al. (2022).

The CH_3OH, HCOOH and PAN columns from IASI presented in this study were retrieved using a neural network that assumed a vertical distribution of each target species in an averaged transport regime, peaking in the free troposphere (see Franco et al., 2018). These vertical assumptions are unfortunately not fully representative for a concentrated fire plume at high altitude, such as observed in the fire event studied here (the altitude of the plume is discussed in Section 3.3.1). As a result, the retrieved columns of CH_3OH, HCOOH and PAN are likely overestimated. In contrast, the more recent ANNI C_2H_4 retrievals from IASI allow accounting specifically for the high altitude of the fire plume (Franco et al., 2022). Using the flexibility of these retrievals, we assess that the other retrieved VOC columns can be overestimated by up to 60% in the fire plume due to the assumption on the fire plume altitude. However, the same type of overestimation affects also the retrieved CO column measurements from IASI. As FORLI retrievals are strongly constrained, they do not allow retrieving the altitude of the fire plume and the typical retrieved profile of CO is mixed vertically, even in the fire plume (George et al., 2015; Hurtmans et al., 2012). As a result, most of these high biases likely cancel in the IASI VOC:CO ratios that are calculated further in this study.

2.4. GEOS-Chem Chemical Transport Model

The GEOS-Chem CTM (www.geos-chem.org; Bey et al., 2001), version 13.3.2, with detailed tropospheric and stratospheric chemistry was used. All model simulations in this study were performed using a horizontal resolution of 2° × 2.5°, with 47 vertical hybrid levels from the surface to 0.01 hPa. The model is driven by assimilated meteorological fields from the Modern-Era Retrospective analysis for Research and Applications, version 2 (MERRA-2; Gelaro et al., 2017), which is provided by the Global Modeling and Assimilation Office (GMAO) at NASA Goddard Space Flight Center. A model spin-up was performed from the beginning of January 2016 to the end of December 2016, before running the full year of 2017, with the last year used for the analysis presented here. Transport and chemical operator time steps of 10 and 20 min, respectively, were selected to minimize simulation errors (Philip et al., 2016).

Starting with GEOS-Chem version 13.1.0, all emissions in the model are configured at run-time using the Harmonized Emissions Component 3.0 (HEMCO; Lin et al., 2021) and various inventories. Global anthropogenic trace gas and aerosol emissions are sourced from the Community Emissions Data System (CEDS; Hoesly et al., 2018) version 2, while biogenic emissions are provided by the Model of Emissions of Gasses and Aerosols from Nature (MEGAN; Guenther et al., 2012) version 2.1. Biomass burning emissions from the Global Fire Assimilation System (GFAS; Kaiser et al., 2012) version 1.2 were used. GFAS provides global emissions for open fires on a

$0.1° \times 0.1°$ grid at 3-hourly resolution, which are derived from assimilated measurements of fire radiative power (FRP) from the Moderate Resolution Imaging Spectroradiometer (MODIS) onboard the NASA Aqua and Terra satellites. All emissions are re-gridded internally from their native resolutions to the $2° \times 2.5°$ model resolution by the HEMCO module. GFAS was selected rather than the Global Fire Emissions Database (GFED) because it better represented the spatial and temporal patterns of the emissions from the 2017 fires when compared with IASI observations (i.e., GFED began emitting much earlier in August than GFAS). Emissions of HCOOH are not included in the current version of GFAS, so in order to approximate these emissions, we scaled the GFAS CO emissions by the ratio of the emissions factors (i.e., EF_{HCOOH}/EF_{CO}, in molar units) taken for boreal forests from Andreae (2019), and then assigned these emissions to HCOOH for the August 2017 fire period. Additionally, C_2H_4 was recently added to GEOS-Chem chemical mechanism in version 13.3.0, and this is possibly the first application of this new simulation to wildfire studies, providing an opportunity to compare the performance of the model against ground- and space-based observations.

3. Results and Discussion

3.1. Observed Enhancements

3.1.1. PEARL-FTIR Time-Series

The total column time series for CO, PAN, C_2H_4, CH_3OH, and HCOOH retrieved from the PEARL-FTIR for the 2006–2020 period at Eureka are shown in Figure 1, along with monthly means. A similar figure to Figure 1 but with measurements from each year differentiated to better highlight previous enhancements is provided as Figure S2 in Supporting Information S1. The largest mean CO columns typically occur during February and March, with minima during July, as seen in Figure 1a. The main sources of CO are fossil fuel combustion and the oxidation of VOCs and CH_4, and it is primarily transported to the Arctic from mid-latitude sources, with biomass burning being a significant secondary source during the summer months (Holloway et al., 2000; Yurganov, 1997). The main sink of CO in the Arctic is the oxidation reaction with OH. Due to the absence of sunlight during the polar night, no OH is produced and the atmospheric lifetime of CO is extended significantly (Holloway et al., 2000). This allows transported mid-latitude CO emissions to accumulate in high concentrations, and leads to the large observed total columns in the spring months (Holloway et al., 2000; Stohl, 2006). With the return of sunlight and the resumption of OH photolysis at the end of polar night, CO columns gradually decrease toward the summer months. The mean column increases in August, when the influence of biomass burning is most prominent.

From Figure 1b, the largest mean PAN total columns are observed in the springtime, with a maxima in April and a minima in July. The main source of PAN to the Arctic is long-range transport from polluted mid-latitude regions where it is formed via the reaction of NMVOCs with NO_x (Beine & Krognes, 2000). The primary sink of PAN is thermal decomposition (Fischer et al., 2014; Tuazon et al., 1991), with a smaller secondary sink due to photolysis that is thought to dominate in the upper troposphere above 7 km (Talukdar et al., 1995). The cold and stable atmosphere during the polar night coupled with the lack of removal processes can lead to an accumulation of transported PAN, resulting in the large observed total columns in the spring months, as seen in Figure 1b, which coincides with the "Arctic haze" pollution phenomenon (Beine & Krognes, 2000; Law et al., 2014; Law & Stohl, 2007). Once the atmosphere begins to warm in the spring, PAN concentrations begin to decrease, leading to smaller measured columns in the summer months. Biomass burning presents a significant contribution to Arctic PAN columns during the summertime, leading to an increase in the mean columns in August that is reflected in the time-series in Figure 1b (Fischer et al., 2014; Tereszchuk et al., 2013). As a result, although it has differing sources and sinks, PAN presents a similar seasonal cycle at Eureka as CO.

Figure 1c shows that there is no detectable seasonal cycle for C_2H_4 columns at Eureka. In general, the column abundances of C_2H_4 at Eureka are extremely low, with mean total columns of 6.45×10^{14} molec. cm^{-2} calculated over all years. Globally, the primary sources of C_2H_4 are biomass burning (approximately 50% of global emissions), anthropogenic emissions from the petrochemical industry, automotive emissions, garbage incineration, and a smaller component from biogenic emissions (Folberth et al., 2006; Gentner et al., 2013; Sawada & Totsuka, 1986). In the Arctic region, there is in essence no significant local source of C_2H_4, and due to its extremely short lifetime (approximately 14–35 hr in the Arctic summer atmosphere) resulting from its high reactivity with OH and O_3, transported mid-latitude anthropogenic emissions present a negligible contribution to Arctic C_2H_4 concentrations (Alvarado et al., 2011; Dolan et al., 2016). Transported biomass burning emissions

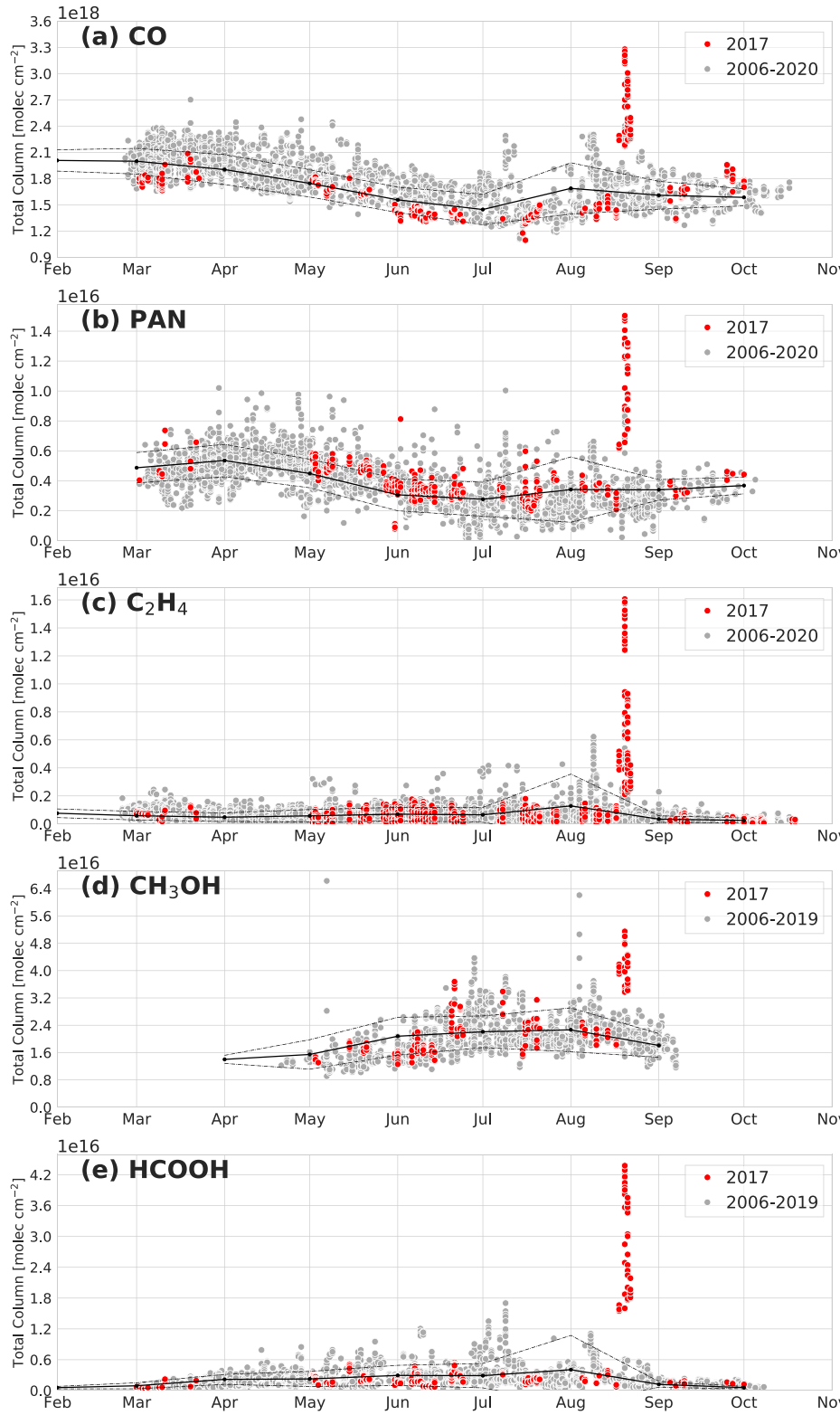

Figure 1. Total column time series of CO, PAN, C_2H_4, CH_3OH, and HCOOH retrieved from the PEARL-FTIR at Eureka for the period of 2006–2020. All years are plotted in light gray, while 2017 is highlighted in red. The solid black line denotes the monthly mean total columns calculated over all years and the dashed black line indicates $\pm 1\sigma$ from the monthly mean.

appear to be the largest driver of the observed annual cycle of C_2H_4 at Eureka, with notable enhancements above the baseline visible in the time-series in Figure 1c from previously detected Canadian and Siberian fires in 2014 and 2016, respectively (Lutsch et al., 2016, 2020).

At Eureka, a clear seasonal cycle of CH_3OH total columns can be seen in Figure 1d, with the smallest total columns during the springtime and the largest columns in July and August, which is in agreement with ACE-FTS observations in Dufour et al. (2007). However, the exact nature of local sources and sinks of CH_3OH in the Arctic are not currently well understood. CH_3OH is primarily emitted biogenically from plants during their growth and decay phase (Ashworth et al., 2016; Fall & Benson, 1996; Hüve et al., 2007; MacDonald & Fall, 1993), with smaller sources including the reaction of methylperoxy radicals (CH_3O_2) with themselves and other organic peroxy radicals, oceanic emissions (Bates et al., 2021), as well as biomass burning (Akagi et al., 2013; Dufour et al., 2006). Its primary sinks are the reaction with OH, surface deposition, and uptake by the ocean (Bates et al., 2021; Stavrakou et al., 2011). A recent model study by Bates et al. (2021) indicates that atmospheric production via the reaction of $CH_3O_2 + CH_3O_2/RO_2$ and biogenic emissions are a significant driver of the seasonal cycle, resulting in a peak in the observed total columns in July and August. Despite this, chemical transport models have been shown to consistently underestimate CH_3OH concentrations, with the largest biases present at high latitudes, suggesting a significant and ubiquitous unknown source (Bates et al., 2021; Chen et al., 2019). Transported biomass burning emissions also influence the Arctic CH_3OH budget during the summer months, although to a lesser degree than biogenic emissions (Dufour et al., 2007).

In the case of HCOOH, the seasonal cycle at Eureka is relatively weak as seen in Figure 1e, however, some seasonality is apparent in the time-series, with smaller total columns in the spring and fall, and larger total columns during the summer. The sinks of HCOOH are believed to be properly constrained, with dry/wet deposition being the primary sink, however the sources of HCOOH in the Arctic are not particularly well understood (Mungall et al., 2018; Paulot et al., 2011). Similar to CH_3OH, previous comparisons of HCOOH observations with models (including GEOS-Chem) show significant underestimations in HCOOH abundances particularly at high northern latitudes, which suggests missing chemistry or unknown sources (Paulot et al., 2011; Schobesberger et al., 2016; Stavrakou et al., 2012). In situ measurements of HCOOH concentrations by Mungall et al. (2018) at Alert, Nunavut (82.30°N, 62.22°W) showed a high degree of diurnal variability and suggest a complex variety of regional sources in the Arctic that vary with meteorological conditions including snow melt emissions, soil emissions, and plant/vegetation emissions. The Eureka time-series demonstrates that biomass burning is a significant source of HCOOH to the high Arctic and a clear driver of the annual cycle, with the largest short-term perturbations in the total columns being the result of biomass-burning-related enhancements. The impact that these transient injections of high HCOOH concentrations to the Arctic atmosphere might have on soil and rainwater acidity should be investigated in future studies.

Enhancements in CO, CH_3OH and HCOOH columns resulting from biomass burning have been observed in the past by the PEARL-FTIR at Eureka, with notable events including the August 2010 Russian fires (Viatte et al., 2013, 2015), the August 2014 NWT wildfires (Lutsch et al., 2016), and the July 2015 Alaskan wildfires (Lutsch et al., 2020). Lutsch et al. (2019) found that the August 2017 Canadian wildfires led to the greatest observed enhancements of CO, NH_3, HCN and C_2H_6 at Eureka in the 2006–2017 time-series. Importantly, it should be noted that all of the largest wildfire-driven enhancements observed at Eureka have occurred in the latter half of the time-series (evident in Figure S2 in Supporting Information S1), suggesting that biomass burning is becoming an increasingly significant source of these reactive trace gases to the high Arctic during the summer months. During the August 2017 fire period, with the exception of CH_3OH, all of the VOC species along with CO exhibited the largest enhancements in their total columns over the whole 2006–2020 Eureka time-series. The observed enhancement reaches a peak on 19 August 2017, with maximum total column values of $3.28 \times 10^{18} \pm 8.67 \times 10^{16}$ molec. cm^{-2}, $1.50 \times 10^{16} \pm 1.32 \times 10^{15}$ molec. cm^{-2}, $1.61 \times 10^{16} \pm 1.15 \times 10^{15}$ molec. cm^{-2}, $5.15 \times 10^{16} \pm 5.62 \times 10^{15}$ molec. cm^{-2}, and $4.38 \times 10^{16} \pm 3.32 \times 10^{15}$ molec. cm^{-2} (total column ± measurement uncertainty) for CO, PAN, C_2H_4, CH_3OH, and HCOOH, respectively. It should be noted that no measurements were available on 18 August 2017 due to poor weather conditions, and it is possible that the PEARL-FTIR did not capture the full extent of this enhancement event. These peak column values represent a perturbation on the order of approximately 2–12 times above the mean August total columns for these species at Eureka. In the case of CH_3OH, the total columns resulting from the 2017 fires are dwarfed by an un-attributed short-term enhancement that occurred in early May 2009, as well as an enhancement that is linked to boreal North American fires in

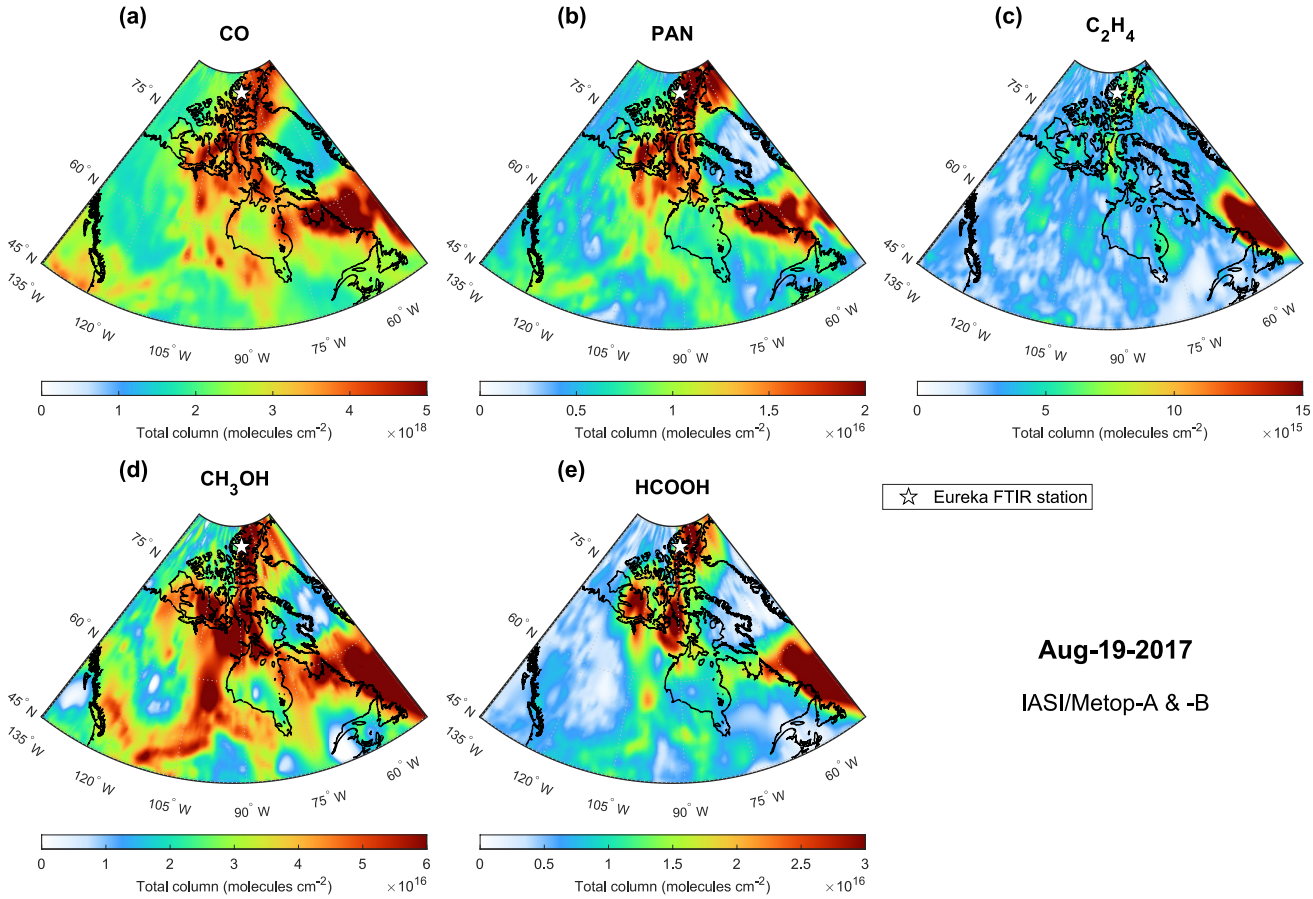

Figure 2. Daily average IASI-A and IASI-B total column measurements of (a) CO, (b) PAN, (c) C_2H_4, (d) CH_3OH, and (e) HCOOH over the mid- and high-latitude regions of North America on 19 August 2017. The location of Eureka, Nunavut is denoted by the white star in the top of each panel.

August 2009 (Lutsch et al., 2020). In the following section, we will discuss the IASI observations over the Arctic during the August 2017 fire period.

3.1.2. IASI Observations

Under typical measurement conditions, retrievals of reactive VOCs from IASI over the high Arctic are difficult due to the low or even negative thermal contrast between the surface and the air directly above it, resulting in weaker signals in the recorded radiances, and hence in larger retrieval errors (Franco et al., 2018). Despite this, elevated concentrations of the target gases and the altitude of the transported plumes from the August 2017 fires provided sufficient sensitivity during the fire-affected period to allow for low-noise observations of these species over the Arctic region. A daily average of CO, PAN, C_2H_4, CH_3OH, and HCOOH observations from IASI-A and IASI-B over the Arctic region on 19 August 2017 (the day of the peak measured enhancement of the PEARL-FTIR) are shown in Figure 2, and an animation of these measurements over the period of 12–24 August is provided as Movie S1. IASI-A and IASI-B observations display strong enhancements in each species in the vicinity of Eureka, and capture the full spatial extent of the plume as it was transported from the Canadian fires northward to the Arctic region. IASI measurements show the plume passing directly over Eureka on 18 and 19 August 2017, corresponding with the peak in the PEARL-FTIR total column measurements. The maximum hourly-mean columns observed by the IASI instruments of CO, PAN, C_2H_4, CH_3OH, and HCOOH on 19 August 2017 within 150 km of Eureka are $4.31 \times 10^{18} \pm 8.44 \times 10^{17}$, $2.45 \times 10^{16} \pm 5.72 \times 10^{15}$, $6.95 \times 10^{15} \pm 3.40 \times 10^{15}$, $6.10 \times 10^{16} \pm 1.94 \times 10^{16}$, and $2.57 \times 10^{16} \pm 5.83 \times 10^{15}$ respectively (mean total column $\pm$ standard deviation). These values broadly agree with the maximum total columns measured by the PEARL-FTIR, although the total columns of the VOC species from IASI are on-average biased lower than those from the PEARL-FTIR. In particular, the observed peak C_2H_4 columns from IASI are significantly smaller than

those from the ground-based instrument ($6.95 \times 10^{15} \pm 3.40 \times 10^{15}$ molec. cm^{-2} vs. $1.61 \times 10^{16} \pm 1.15 \times 10^{15}$ molec. cm^{-2} from the PEARL-FTIR). Relative to ground-based FTIR measurements, the vertical sensitivity of the IASI VOC retrievals may be reduced due to the aforementioned thermal contrast issues, potentially contributing to differences in the measured total columns. However, since ANNI retrievals do not employ an OEM-based approach, they do not produce averaging kernels, making it difficult to diagnose any differences in the vertical sensitivities between the instruments (Franco et al., 2018).

Additionally, the IASI observations shown in Figure 2 provide a clear picture of the fragmentation of the biomass burning plume. A large portion of the plume can be seen passing over Eureka and the high Arctic, while another substantial fragment of the plume (centered around 60°N) is shown being lofted eastward toward the Atlantic Ocean and Europe, where it contributed to a stratospheric smoke layer and enhanced aerosol optical depth measurements over western Europe (Khaykin et al., 2018). The transported plumes from the BC and NWT fires resulted in the largest C_2H_4 total columns, and the second largest PAN total columns measured on 20 August 2017 by a Bruker 120HR ground-based FTIR at Jungfraujoch, Switzerland (46.55°N, 7.98°E, 3580 m a.s.l) which has been in operation since 1995. A time-series of C_2H_4 total columns measured at Jungfraujoch with the observations from 20 August 2017 highlighted is provided in the Figure S3 in Supporting Information S1. The smoke from the August 2017 fires persisted in the stratosphere above Europe for several months, and the magnitude of the smoke injection has since been likened to that of a moderate volcanic eruption, demonstrating the exceptional nature of this particular fire event (Khaykin et al., 2018; P. Yu et al., 2019). In the following section, we will discuss the trace gas correlations, emission ratios, and emission factors that have been derived from PEARL-FTIR and IASI measurements, as well as contrast them with the values provided in the literature.

3.2. Emissions Estimates

3.2.1. Trace Gas Correlations

The enhancement ratio (EnhR) enables a quantification of trace-gas emissions from biomass burning during wildfire events. Fire-affected measurements were first identified by those which had total column amounts greater than 1σ standard deviation from the monthly mean of all measurements and over all years following the methods of Lutsch et al. (2016, 2019), and Viatte et al. (2015). Due to the fact that the FTIR measurements are made across various spectral regions using a series of optical filters (i.e., CO and the VOCs may not be measured simultaneously), we only pair CO and VOC measurements made within 1 hr of each other, with each CO measurement only being used once. The 1-hr window was selected following the approach of Lutsch et al. (2019) to maximize the number of measurement pairs, while simultaneously minimizing the effects of plume aging between paired observations. On average, the difference in measurement times for each species and the coincident CO measurement is approximately 20 min. The EnhR (in units of molec. cm^{-2}/molec. cm^{-2}) is then given by the slope of a linear least-squares regression between the target species and CO for all fire-affected measurements. It should be noted that the FTIR measurements have systematic (non-random) uncertainties (see Table 2); so to properly account for this, bootstrap resampling (with 5000 ensemble members) was used to determine the 95% confidence intervals as the uncertainties for the fitted slopes. Bootstrap resampling such as this allows for a robust treatment of non-normally distributed datasets (Gatz & Smith, 1995). This process was repeated using IASI-A and IASI-B measurements within 150 km of Eureka to provide a second set of EnhRs for comparison with the values derived from the PEARL-FTIR. The trace-gas correlations for each VOC species versus CO for the PEARL-FTIR are shown in Figure 3, and the resulting enhancement ratios are provided in the fourth column of Table 3. A similar figure as Figure 3 but for IASI is shown in Figure S4 in Supporting Information S1. Enhancement ratios are sensitive to plume travel times, particularly for short-lived species (Viatte et al., 2015). As a result, comparisons with previously reported EnhRs from the literature can be challenging. However, for completeness we have included values from previous studies in Table 3 wherever they were available.

PAN, C_2H_4, CH_3OH, and HCOOH display strong correlations with CO during the fire-affected period of 17–23 August 2017, with Pearson correlation coefficients of $R = 0.91$, $R = 0.97$, $R = 0.73$, and $R = 0.96$, respectively. In the case of CH_3OH, the smaller correlation coefficient may be due in part to the smaller number of observations during the fire period and the weaker overall enhancement relative to the other VOC species. However, this is consistent with Viatte et al. (2015) who found CH_3OH to have generally weaker correlations with CO than most other biomass burning tracer species at Eureka. The linear regressions obtained from IASI measurements for PAN, C_2H_4, CH_3OH, and HCOOH display good to moderate correlations with CO with $R = 0.87$, $R = 0.68$,

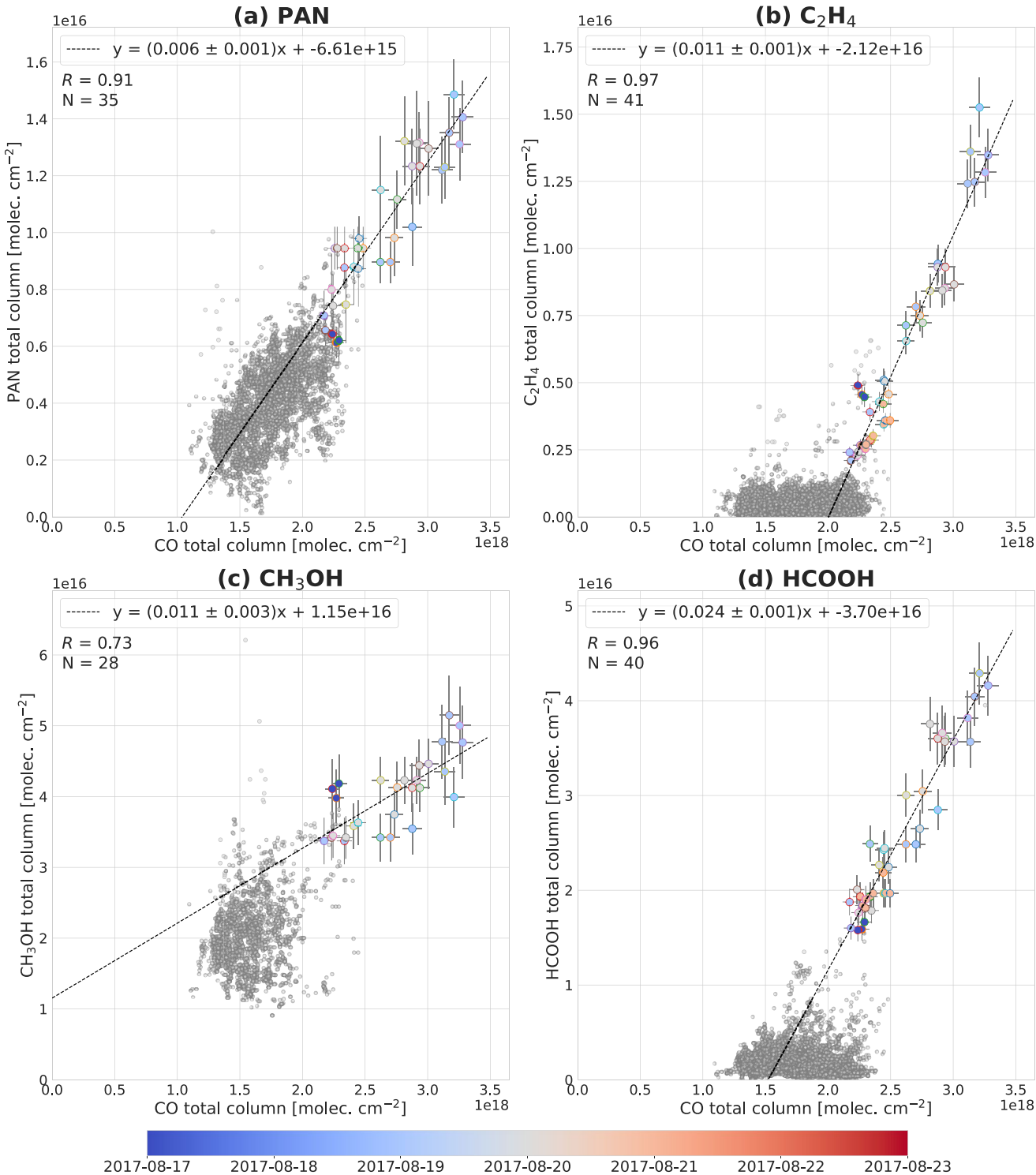

Figure 3. Enhancement ratios derived from PEARL-FTIR measurements of (a) PAN, (b) C_2H_4, (c) CH_3OH, and (d) HCOOH relative to CO during the fire-affected period of 17–23 August 2017. Data points from the fire period are colored based on the day on which the measurements were made, and all other measurements (from 2006 to 2020) are plotted in light gray. The equation for the linear fit, the Pearson correlation coefficient *R*, and the number of fire-affected measurements are shown in the upper left of each panel.

Table 3
Comparison of Calculated Enhancement Ratios, Emission Ratios, and Emission Factors for PAN, C_2H_4, CH_3OH, HCOOH at Eureka

Source	Type	EF_{CO}(g kg^{-1})	EnhR × 10^{-3}	ER × 10^{-3}	EF (g kg^{-1})
PAN					
This study—PEARL-FTIR	Ground-based	-	6.36 (0.65)	-	-
This study—IASI	Satellite	-	5.86 (0.66)	-	-
Tereszchuk et al. (2013)[a]	Satellite	-	3.61 (0.54)	-	-
Alvarado et al. (2010)[b]	Aircraft	-	3.50 (2.60)	-	-
C_2H_4					
This study—PEARL-FTIR	Ground-based	121 (47)[c]	10.6 (0.72)	109 (0.72)	13.2 (5.21)
This study—IASI	Satellite	121 (47)[c]	1.60 (0.37)	16.5 (0.37)	1.99 (0.82)
GFASv1.2[d]	Compilation	106 (37)	-	-	1.18 (0.55)
Andreae (2019)[e]	Compilation	121 (47)	-	-	1.54 (0.66)
Akagi et al. (2011)	Compilation	127 (45)	-	-	1.42 (0.43)
Simpson et al. (2011)[f]	Aircraft	113 (72)	-	7.30 (0.10)	0.82 (0.09)
Goode et al. (2000)[h]	Aircraft	88.8	-	38.4	3.28
CH_3OH					
This study—PEARL-FTIR	Ground-based	121 (47)[c]	10.6 (2.64)	21.2 (2.64)	2.94 (1.51)
This study—IASI	Satellite	121 (47)[c]	10.7 (4.60)	21.4 (4.60)	2.96 (1.79)
GFASv1.2[d]	Compilation	106 (37)	-	-	1.89 (1.40)
Andreae (2019)[e]	Compilation	121 (47)	-	-	2.33 (1.45)
Akagi et al. (2011)	Compilation	127 (45)	-	-	2.82 (1.62)
Viatte et al. (2015)[h]	Ground-based	127 (45)	25.9 (20.6)	28.1 (12.5)	3.44 (1.68)
Tereszchuk et al. (2013)[a]	Satellite	-	1.99 (0.40)	-	-
Rinsland et al. (2007)[i]	Satellite	86 (17)	-	27.8 (4.56)	2.73 (0.71)
Simpson et al. (2011)[f]	Aircraft	113 (72)	-	9.60 (1.90)	1.20 (0.30)
Goode et al. (2000)[g]	Aircraft	88.8	-	15.3	1.45
HCOOH					
This study—PEARL-FTIR	Ground-based	121 (47)[c]	24.3 (1.43)	71.7 (1.43)	14.3 (5.83)
This study—IASI	Satellite	121 (47)[c]	9.47 (1.78)	28.0 (1.78)	5.56 (2.51)
Andreae (2019)[e]	Compilation	121 (47)	-	-	1.04 (0.89)
Akagi et al. (2011)	Compilation	127 (45)	-	-	0.57 (0.46)
Viatte et al. (2015)[h]	Ground-based	127 (45)	8.08 (5.87)	15.3 (4.03)	2.69 (1.14)
Pommier et al. (2017)[j]	Satellite	-	4.40 (0.09)	-	-
R'Honi et al. (2013)[k]	Satellite	-	11.0	47.0	-
Tereszchuk et al. (2013)[a]	Satellite	-	1.46 (0.49)	-	-
Rinsland et al. (2007)[i]	Satellite	86 (17)	-	4.63 (0.67)	0.65 (0.16)
Goode et al. (2000)[g]	Aircraft	88.8	-	11.6	1.57

Note. The reported uncertainties are provided in parentheses.

[a]ACE-FTS observations of Canadian and Alaskan plumes aged by 120–144 hr. [b]NASA DC-8 measurements of aged Canadian boreal plumes during the 2008 ARCTAS-B campaign. [c]To convert from ER to EF in this work, we use the EF_{CO} for boreal forests from Andreae (2019). [d]Emission factors for boreal forests based on Andreae and Merlet (2001) with updates by M.O. Andreae. [e]Values reported for boreal forests. [f]Measurements of Canadian boreal fires during the 2008 ARCTAS-B campaign. [g]Measurements of Alaskan fires. [h]Mean values derived from ground-based FTIR measurements at Eureka, Nunavut between 2008 and 2012. [i]Also ACE-FTS observations of Canadian and Alaskan fires. [j]IASI observations of Siberian boreal fires. [k]IASI measurements of plumes from the 2010 central Russian fires. The EnhR is an average over all days of the fires.

$R = 0.47$, and $R = 0.79$, respectively. IASI measurements show the weakest correlation for CH_3OH with CO, which is consistent with the correlations derived from the PEARL-FTIR measurements. The calculated enhancement ratios from the PEARL-FTIR for PAN, C_2H_4, CH_3OH, and HCOOH relative to CO are $(6.36 \pm 0.51) \times 10^{-3}$, $(10.6 \pm 0.45) \times 10^{-3}$, $(10.6 \pm 1.92) \times 10^{-3}$, and $(24.3 \pm 1.20) \times 10^{-3}$, respectively. These values can be compared with the enhancement ratios derived from IASI-A and IASI-B measurements which are $(5.86 \pm 0.46) \times 10^{-3}$, $(1.60 \pm 0.24) \times 10^{-3}$, $(10.7 \pm 3.53) \times 10^{-3}$, and $(9.46 \pm 1.46) \times 10^{-3}$ for PAN, C_2H_4, CH_3OH, and HCOOH relative to CO, respectively. For CH_3OH and PAN, the PEARL-FTIR and IASI measurements yield identical enhancement ratios. The CH_3OH enhancement ratios can be roughly compared with Viatte et al. (2015), who obtained a mean CH_3OH:CO ratio of $(25.9 \pm 20.6) \times 10^{-3}$ across all fire events detected at Eureka between 2008 and 2012. The mean value from Viatte et al. (2015) is more than double the values from the PEARL-FTIR and IASI in this study, however our values fall within their bounds of uncertainty.

Since ground-based FTIR retrievals of PAN are new, there were no ground-based studies available for comparison. However, ACE-FTS measurements over aged Canadian and Alaskan plumes by Tereszchuk et al. (2013) yielded a PAN enhancement ratio of $(3.61 \pm 0.54) \times 10^{-3}$, and while this value is quite close to the enhancement ratios in this study, they fall just outside of the bounds of error. Aircraft measurements of aged Canadian boreal plumes during the ARCTAS-B campaign by Alvarado et al. (2010) yielded a mean PAN enhancement ratio of $(3.50 \pm 2.60) \times 10^{-3}$, with a range of individual PAN:CO enhancement ratios between 1.10×10^{-3} to 8.70×10^{-3}. While their reported mean value is smaller than the ones measured in this study as well as those reported by Tereszchuk et al. (2013), our values from the PEARL-FTIR and IASI fall inside their range of reported enhancement ratios, and the upper bound of their mean value when accounting for the uncertainty.

For C_2H_4 and HCOOH, there are large differences in the EnhRs from the PEARL-FTIR and IASI. The C_2H_4 EnhR from PEARL-FTIR measurements is an order of magnitude larger than the one derived from IASI ($(10.6 \pm 0.45) \times 10^{-3}$ vs. $(1.60 \pm 0.24) \times 10^{-3}$, respectively). The difference in the HCOOH EnhRs is smaller, but the FTIR-derived value is more than twice the IASI-derived EnhR ($(24.3 \pm 1.20) \times 10^{-3}$ vs. $(9.47 \pm 1.46) \times 10^{-3}$, respectively). It should be noted however, that the IASI-derived EnhR for HCOOH of $(9.47 \pm 1.46) \times 10^{-3}$ is independently larger than the mean EnhR of $(8.08 \pm 5.87) \times 10^{-3}$ derived from ground-based FTIR measurements for all fires detected at Eureka between 2008 and 2012 provided by Viatte et al. (2015). The low bias in the IASI EnhRs for C_2H_4 and HCOOH is related to the smaller retrieved mean total columns for these species relative to the PEARL-FTIR, which is likely a result of the generally lower sensitivity of the IASI retrievals and the poor observational conditions for IASI.

3.2.2. Calculation of Emission Ratios and Emission Factors

Since the FTIR and IASI measurements at Eureka are being made at a significant distance from the fire sources, the transported biomass burning plumes have undergone chemical aging, which leads to some loss of each species. We can correct the EnhRs to account for the plume travel time and the subsequent chemical aging by calculating the equivalent emission ratio (ER) at the fire source. The ER is given by (Lutsch et al., 2016; Viatte et al., 2015):

$$\mathrm{ER}_X = \mathrm{EnhR}_X \cdot \left(\frac{\exp\left(\frac{t}{\tau_x}\right)}{\exp\left(\frac{t}{\tau_{\mathrm{co}}}\right)} \right), \tag{1}$$

where τ_x is the lifetime of the target species, and t is the travel time of the plume. For CO, an atmospheric lifetime of 30 days was chosen based on Viatte et al. (2015), who performed model comparisons with FTIR measurements at Eureka. For C_2H_4, CH_3OH, and HCOOH, atmospheric lifetimes of 2, 5.8 and 4 days were chosen based on Stavrakou et al. (2011, 2012), and Toon et al. (2018), respectively. For the calculation of the ERs, a plume travel time of 5 days was selected based on the FLEXPART model back-trajectories described in Lutsch et al. (2020).

Additionally, biomass burning emissions are often characterized using the emission factor (EF), which quantifies the amount of a given trace-gas species emitted per kg of dry biomass combusted (in units of g kg^{-1}). Emission factors are commonly reported in the literature, allowing for direct comparisons with the values derived in this study. The emission factor is defined as (Andreae, 2019; Andreae & Merlet, 2001):

$$\mathrm{EF}_X = \mathrm{EF}_{\mathrm{co}} \cdot \mathrm{ER}_X \cdot \left(\frac{\mathrm{MW}_X}{\mathrm{MW}_{\mathrm{co}}} \right), \tag{2}$$

where MW is the molecular weight of a given species (in units of g mol^{-1}). To convert from our calculated emission ratios to emission factors, we use the emission factor for CO of 121 ± 47 g kg^{-1} for boreal forests from the most recent compilation study by Andreae (2019). The uncertainty in the calculated emission factors is determined by adding the relative uncertainty contributions from the emission ratio of each respective species, and the CO emission factor. The calculated emission ratios and emission factors for the PEARL-FTIR and IASI, as well as those collected from previous studies are provided in columns 5 and 6 of Table 3, respectively. Additionally, the emission factors of CO used in the calculations of the emission ratios and emission factors are provided in column 3 of Table 3 where available. For PAN, since it only results from secondary formation, we do not calculate the emission ratio or emission factor.

From the measured C_2H_4 enhancement ratio, we obtain emission ratios of (109 ± 0.72) × 10^{-3} and (16.5 ± 0.37) × 10^{-3} for the PEARL-FTIR and IASI, respectively. The derived emission factors are 13.2 ± 5.21 g kg^{-1} from the PEARL-FTIR, and 1.99 ± 0.82 g kg^{-1} from IASI, reflecting a difference of approximately 560% in the emission factors. The emission factor computed from the FTIR is an order of magnitude larger than those provided by the compilation studies by Akagi et al. (2011) and Andreae (2019), as well as the value used in GFASv1.2, which give emission factors of 1.54 ± 0.66 g kg^{-1}, 1.42 ± 0.43 g kg^{-1}, and 1.18 ± 0.55 g kg^{-1}, respectively. Furthermore, aircraft measurements by Simpson et al. (2011) over Canadian boreal fires during the 2008 ARCTAS-B campaign yielded an emission factor for C_2H_4 of 0.82 ± 0.09 g kg^{-1}, while aircraft measurements over Alaskan fires by Goode et al. (2000) yielded an emission factor of 3.28 (with no uncertainty reported), both of which are significantly smaller than the value obtained from the FTIR in this study. The C_2H_4 emission factor of 1.99 ± 0.81 obtained from IASI measurements in this study is larger than all previous studies with the exception of Goode et al. (2000), and only overlaps within the bounds of uncertainty of the reported value of Andreae (2019). As previously discussed in Sections 3.1.2 and 3.2.1, limitations in the measurement sensitivity of the IASI retrievals over the high Arctic compared to the ground-based FTIR may lead to the satellite measurements not capturing the full magnitude of the enhancement in the total column abundances, and may contribute to the observed difference in the derived emission factors and emission ratios compared to the FTIR results.

In the case of CH_3OH, there is extremely good agreement between the derived emission ratios and emission factors from the PEARL-FTIR and IASI. The emission ratios are (21.2 ± 2.64) × 10^{-3} and (21.4 ± 4.60) × 10^{-3} for the PEARL-FTIR and IASI, respectively. These emission ratios yield emission factors of 2.94 ± 1.51 g kg^{-1} for the PEARL-FTIR, and 2.96 ± 1.79 g kg^{-1} for IASI. The derived emission factors in this study agree well with the values from the two most recent compilation studies by Akagi et al. (2011) and Andreae (2019), who reported values of 2.33 ± 1.45 g kg^{-1} and 2.81 ± 1.62 g kg^{-1}, respectively. PEARL-FTIR and IASI emission factors are both larger than the GFASv1.2 emission factor of 1.89 ± 1.40 g kg^{-1}, which falls toward the lower end of the literature values, however, this value is based on Andreae and Merlet (2001) and is likely out-dated in comparison to the newer study by Andreae (2019). Viatte et al. (2015) reported a mean CH_3OH emission factor of 3.44 ± 1.68 g kg^{-1} across all fires at Eureka between 2008 and 2012, which is larger than the values derived in this study, but still agrees within the combined bounds of uncertainty. A study by Rinsland et al. (2007) that used ACE-FTS satellite observations of Canadian and Alaskan fires provides an emission factor of 2.73 ± 0.71 g kg^{-1}, which is in agreement with our values, and falls between the values provided in the compilation studies by Akagi et al. (2011) and Andreae (2019). Lastly, studies by Goode et al. (2000) and Simpson et al. (2011) using aircraft measurements reported smaller emission factors of 1.2 ± 0.3 g kg^{-1} and 1.45 g kg^{-1}, respectively, which do not agree within the bounds of uncertainty of our values. In general, our CH_3OH emission factors fall toward the upper end of the values reported in the literature, but show excellent agreement with recent studies.

For HCOOH, the calculated emission ratio from the PEARL-FTIR is (71.7 ± 1.43) × 10^{-3}, which is notably larger than the emission ratio of (28.0 ± 1.78) × 10^{-3} determined from IASI measurements. The resulting emission factors display similar differences, with values of 14.3 ± 5.83 g kg^{-1} and 5.56 ± 2.51 g kg^{-1} for the PEARL-FTIR and IASI, respectively, reflecting a difference of approximately 150%. In comparison to the HCOOH emission ratios and factors previously reported in the literature, both of the values derived in this study are significantly larger. One exception to this is R'Honi et al. (2013) who obtained a mean emission ratio for HCOOH of 47.0 × 10^{-3} using IASI measurements over plumes from the 2010 central Russian wildfires, which falls in between the values derived from PEARL-FTIR and IASI in this study. The compilation studies by Akagi et al. (2011) and Andreae (2019) provide emission factors of 1.04 ± 0.89 g kg^{-1} and 0.57 ± 0.46, respectively, which are roughly 1/10th and 1/20th of the emission factor from the FTIR, and 1/5th and 1/10th of the emission factor from IASI in this study. The ground-based study by Viatte et al. (2015) reported a mean emission factor

for HCOOH of 2.69 ± 1.14, which is larger than the aforementioned compilation studies, but is still significantly smaller than the values in this study. It should be noted, however, that for one particularly large enhancement event in August 2010 resulting from fires in Russia, Viatte et al. (2015) obtained an emission ratio of 40.9×10^{-3}, which falls between the range of the values derived from the PEARL-FTIR and IASI in this work. Rinsland et al. (2007) provide an emission factor of 0.65 ± 0.16 g kg^{-1}, which is in-line with Akagi et al. (2011), but is smaller than this study and the other previous studies listed in Table 3. Lastly, aircraft measurements by Goode et al. (2000) in Alaskan fire plumes yielded an emission factor for HCOOH of 1.57 g kg^{-1}, which is larger than the values from the studies by Akagi et al. (2011), Andreae (2019), and Rinsland et al. (2007), but is still significantly smaller than the derived emission factors from IASI and the PEARL-FTIR in this study. The high emission ratio and emission factor calculated for HCOOH may indicate that significant secondary production of this species occurred in the plumes. This will be investigated further using GEOS-Chem sensitivity tests in Section 3.3.2.

3.3. GEOS-Chem Comparisons to Observations

3.3.1. Simulated Plume Transport and Enhancement

Since measurements of reactive VOC species are sparse in the high-Arctic region, global chemical transport models such as GEOS-Chem can provide an additional perspective on the transport and enhancements resulting from wildfires in these remote regions. Furthermore, PEARL-FTIR and IASI measurements of these reactive species can serve as a means for evaluating the performance of the model during this fire event, in particular, for the new C_2H_4 simulation that was recently added to GEOS-Chem in version 13.3.0. In this study, we use CO as a tracer of the wildfire emissions and the subsequent transport since due to its long atmospheric lifetime of approximately 30 days, it is relatively unaffected by chemical aging in the plume over the span of a several days. In comparison, C_2H_4, CH_3OH, and HCOOH all have lifetimes on the order of a few days, and while the lifetime of PAN is highly temperature dependent, its lifetime due to thermal decomposition is generally shorter than that of CO in the troposphere (D. Jacob, 2000; Moxim et al., 1996).

Comparisons of GEOS-Chem simulations with IASI and the PEARL-FTIR were performed as follows. For comparisons with IASI, the IASI data was re-gridded onto the 2° × 2.5° spatial grid used by the model. Since the IASI ANNI retrievals do not produce averaging kernels, we do not apply averaging kernel smoothing in these comparisons. When performing direct comparisons between GEOS-Chem and the PEARL-FTIR, we first select the nearest grid-box of the model to PEARL, and then pair the GEOS-Chem simulated profiles (which are outputted at a two-hour frequency) with FTIR observations within ±1 hr of the time of the FTIR measurement, allowing multiple FTIR measurements to pair with a single GEOS-Chem profile. The GEOS-Chem profiles are interpolated to the FTIR vertical grid, and then smoothed by the mean FTIR total column averaging kernel calculated over all years for the respective species following Rodgers and Connor (2003). The application of averaging kernel smoothing such as this minimizes any biases introduced by the a priori profile and the sensitivity of the instrument, allowing for an optimized comparison between the model and the FTIR measurements. When qualitatively inter-comparing both the PEARL-FTIR and IASI with GEOS-Chem, no smoothing or re-gridding was applied to the GEOS-Chem data.

We first performed a baseline GEOS-Chem simulation for the period of August 2017 with no modifications made to the GFAS emissions or the method through which the emissions were being injected. By default, in version 13 of the model, biomass burning emissions from GFAS are distributed evenly between the surface and the "mean altitude of maximum injection" (MAMI), which is determined using a simple 1-D plume-rise model as described in Freitas et al. (2006) and Rémy et al. (2017). The mean MAMI values during the period of peak fire activity between 10–15 August 2017 for the BC and NWT fires were approximately 1500 and 1100 m, respectively. However, in the case of wildfires such as the 2017 BCE fires where strong pyroCb events occurred, this injection scheme may not properly reflect reality as pyroCb smoke plumes can rise to extreme altitudes before they are transported laterally. Fromm et al. (2021) and Peterson et al. (2018) termed the BC pyroCb event the Pacific Northwest Event (PNE), and demonstrated that the smoke from these fires was injected directly into the lower stratosphere at an altitude of approximately 12–13 km before being lofted northwards, which represents a significant disparity with the values provided by GFAS.

The baseline simulation displays a severe model discrepancy with respect to IASI observations whereby the plume is diverted around Eureka almost entirely, resulting in much smaller enhancements in the total column

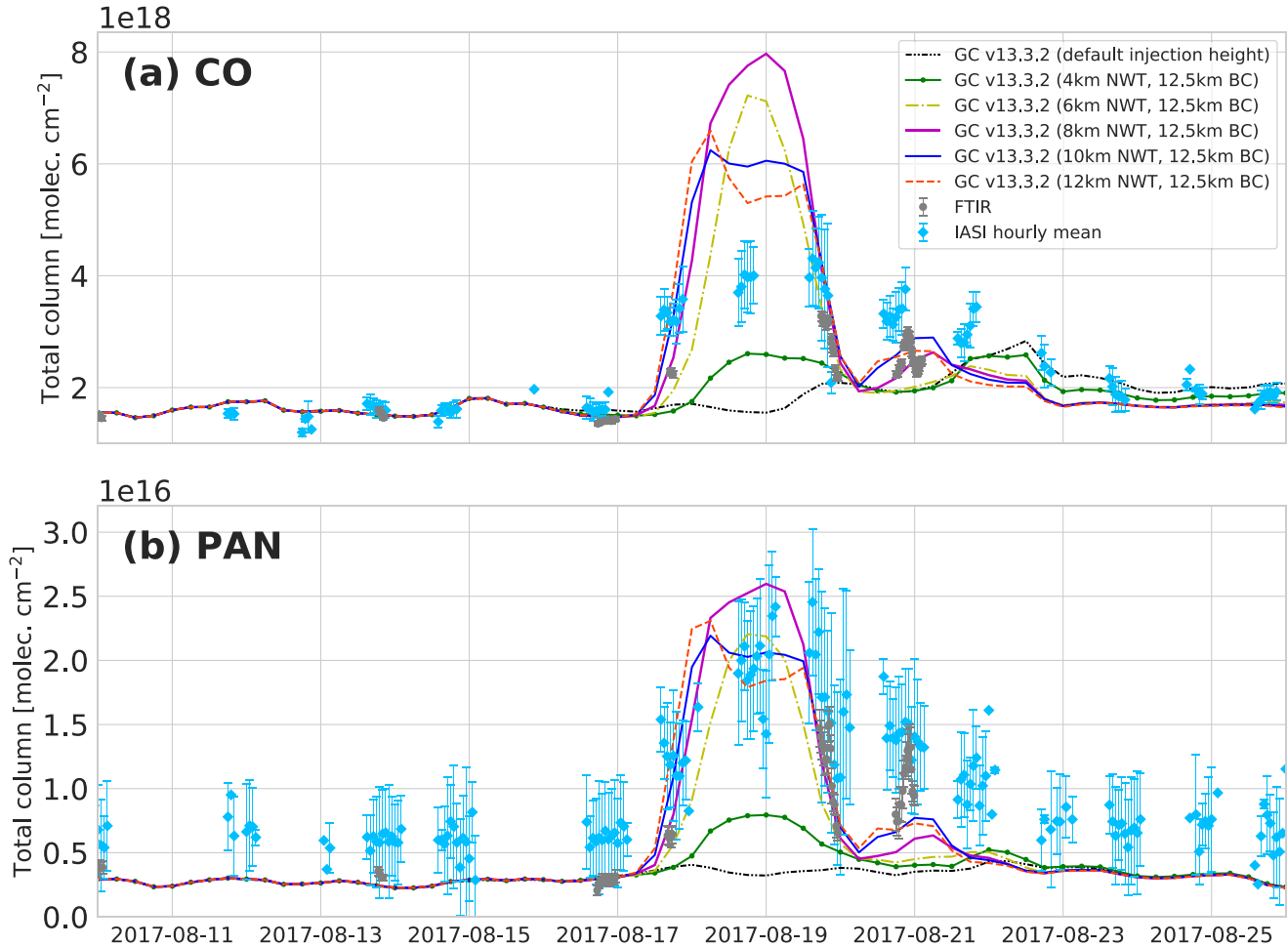

Figure 4. Time-series of un-smoothed GEOS-Chem columns of (a) CO, and (b) PAN for simulations with varying emission injection heights for the NWT wildfires. PEARL-FTIR measurements are shown in gray, and IASI-A and IASI-B hourly averages within 150 km of Eureka are shown in cyan. The error bars on the FTIR data points indicate the measurement uncertainties and the error bars on the IASI data points correspond to the standard deviations.

abundances of CO and the VOC species than was observed by the PEARL-FTIR and IASI. An animation illustrating this transport error in the baseline simulation in relation to re-gridded IASI-A and IASI-B CO measurements is provided as Movie S2. To exclude the possibility that the model error was being introduced by the choice of meteorology, an identical baseline simulation was performed using GEOS-FP meteorology in place of MERRA-2, however both simulations exhibited a nearly identical model error. This model error was determined to be a direct result of the method through which the biomass burning emissions are injected into the vertical model grid. The injection height of the BC fires has been examined in detail in the literature (e.g., Bourassa et al., 2019; Fromm et al., 2021; Peterson et al., 2018; Torres et al., 2020), and it is generally understood that the plume was injected into the UTLS with a mean altitude of 12–13 km above the fires, with the top of the injected plume reaching as high as 13.7 km. However, the injection and plume height of the NWT fires has not been examined in the same depth, and is not well constrained.

To ascertain an appropriate injection height for the NWT fires, we performed a series of simulations with variable injection heights for the NWT fires, while using a fixed injection height of 12.5 km for the BC fires based on Fromm et al. (2021) and Peterson et al. (2018), and we used both CO and PAN as tracers for the plume transport. CO was chosen because its long atmospheric lifetime means that it will be minimally affected by chemical aging over the course of a few days, and PAN was selected as a secondary tracer since it is highly sensitive to the transport altitude as a result of the strong temperature dependence of its atmospheric lifetime. To quantitatively assess the performance of each simulation, we calculated the correlations of the smoothed GEOS-Chem columns with those observed by the PEARL-FTIR. A time-series of GEOS-Chem simulated columns of CO and PAN for the

various injection height simulations, along with PEARL-FTIR observations and hourly-averaged IASI measurements are shown in Figure 4, and correlation plots of GEOS-Chem with the PEARL-FTIR for CO and PAN for each simulation are provided as Figures S5 and S6 in Supporting Information S1. For both CO and PAN, it can be seen from Figure 4 that the simulation using the default GFAS injection height scheme fails to produce a noticeable enhancement in the total columns on 18 and 19 August 2017 when IASI and the PEARL-FTIR observed the peak enhancement. Setting the injection height for the BC fires to 12.5 km and increasing the injection height for the NWT fires to 4 km starts to produce a stronger simulated enhancement at Eureka, however, the magnitude of the resulting enhancement is still smaller than that from both IASI and FTIR observations. Further increasing the NWT injection height leads to a larger subsequent enhancement at Eureka up to a value of approximately 8 km, after which the magnitude of the peak enhancement begins to decrease again. The simulation with a 5 km injection height for NWT matches the magnitude of the peak CO enhancement of IASI most closely, however, this simulation has only a moderate correlation with the PEARL-FTIR measurements of $R = 0.74$ for CO, and $R = 0.70$ for PAN. The strongest correlation between GEOS-Chem and the PEARL-FTIR for both CO and PAN is seen with an injection height for the NWT fires of 10 km, with Pearson correlation coefficients of $R = 0.85$ and $R = 0.77$, respectively. Furthermore, the simulation using a 10 km injection height for the NWT fires reproduces the secondary peak observed in the FTIR measurements on 21 August 2017 most effectively. Although an injection height of 10 km for the NWT fires may be higher than in reality, injecting the emissions at a higher altitude such as this may compensate for the slower vertical transport in the troposphere of the GEOS-Chem model which has previously been highlighted by Stanevich et al. (2020) and K. Yu et al. (2018). For the remainder of the comparisons with observations, we use an injection height of 12.5 km for the BC fires, and 10 km for the NWT fires, and this is referred to as the "modified injection height" simulation.

Figure 5 shows daily-averaged IASI-A and IASI-B measurements re-gridded onto the 2° × 2.5° GEOS-Chem model grid in addition to the simulated columns from the modified injection height simulation for CO, PAN, C_2H_4, CH_3OH, and HCOOH on 19 August 2017. The modified injection height simulation appears to capture the shape and spatial distribution of the plume extremely well in comparison to IASI observations. Furthermore, the GEOS-Chem simulation shown in Figure 5 exhibits a similar pattern of the fragmentation of the plume as seen in IASI observations as discussed in Section 3.1.2. GEOS-Chem shows one fragment being transported northwards toward Eureka, and the other (centered around 60°N, 55°W) that was transported eastwards toward Europe. IASI daily means display larger columns than the model in the eastern plume fragment, which may be a result of numerical diffusion of the plume that has previously been identified as a source of transport errors at coarser horizontal resolutions in the GEOS-Chem model, particularly in the free troposphere (Eastham & Jacob, 2017). The magnitude of the columns in the northern fragment of the plume in GEOS-Chem is in closer agreement with IASI observations, particularly for PAN and CH_3OH. Some differences in the total columns are seen for CO, HCOOH, and C_2H_4, which are overall smaller in the IASI observations than in GEOS-Chem, however this may also be impacted by the lower density of IASI measurements at these high latitudes. Despite this, the GEOS-Chem simulation with the modified injection heights successfully reproduces the spatial and temporal pattern of the plume that is observed by IASI.

The time-series for each species of GEOS-Chem simulated columns, as well as PEARL-FTIR measurements and IASI observations near Eureka are shown in Figure 6. In the vicinity of Eureka, IASI and GEOS-Chem display comparable PAN total columns, but for all other species, IASI observes smaller total columns than is predicted by GEOS-Chem, particularly during the peak enhancement on 18–19 August 2017. The largest measurement-model difference is seen for C_2H_4, of which only a very small enhancement is seen by IASI near Eureka on 19 August 2017. The observed differences between IASI and the model are likely again related to the reduced sensitivity of the IASI instrument and retrievals over high-latitude regions such as the Arctic. In comparison to the PEARL-FTIR, the GEOS-Chem columns of all species in the baseline simulation are severely underestimated relative to the ground-based measurements, and this simulation fails to capture the temporal pattern of the enhancement. In contrast, the simulated total columns of all species in the modified injection height simulation broadly agree with the magnitude of the columns observed by the PEARL-FTIR on 19 August 2017, the day following peak enhancement observed by IASI. Since no FTIR measurements were taken on 18 August 2017, we lack a third point of comparison, and it is difficult to assess whether the magnitude of the enhancement on that day is being simulated accurately.

More specifically, the GEOS-Chem CO columns on 18 August are approximately 2×10^{18} molec. cm^{-2} (~+50%) larger than the IASI daily mean, and approximately 4×10^{18} molec. cm^{-2} (~+100%) larger than those measured

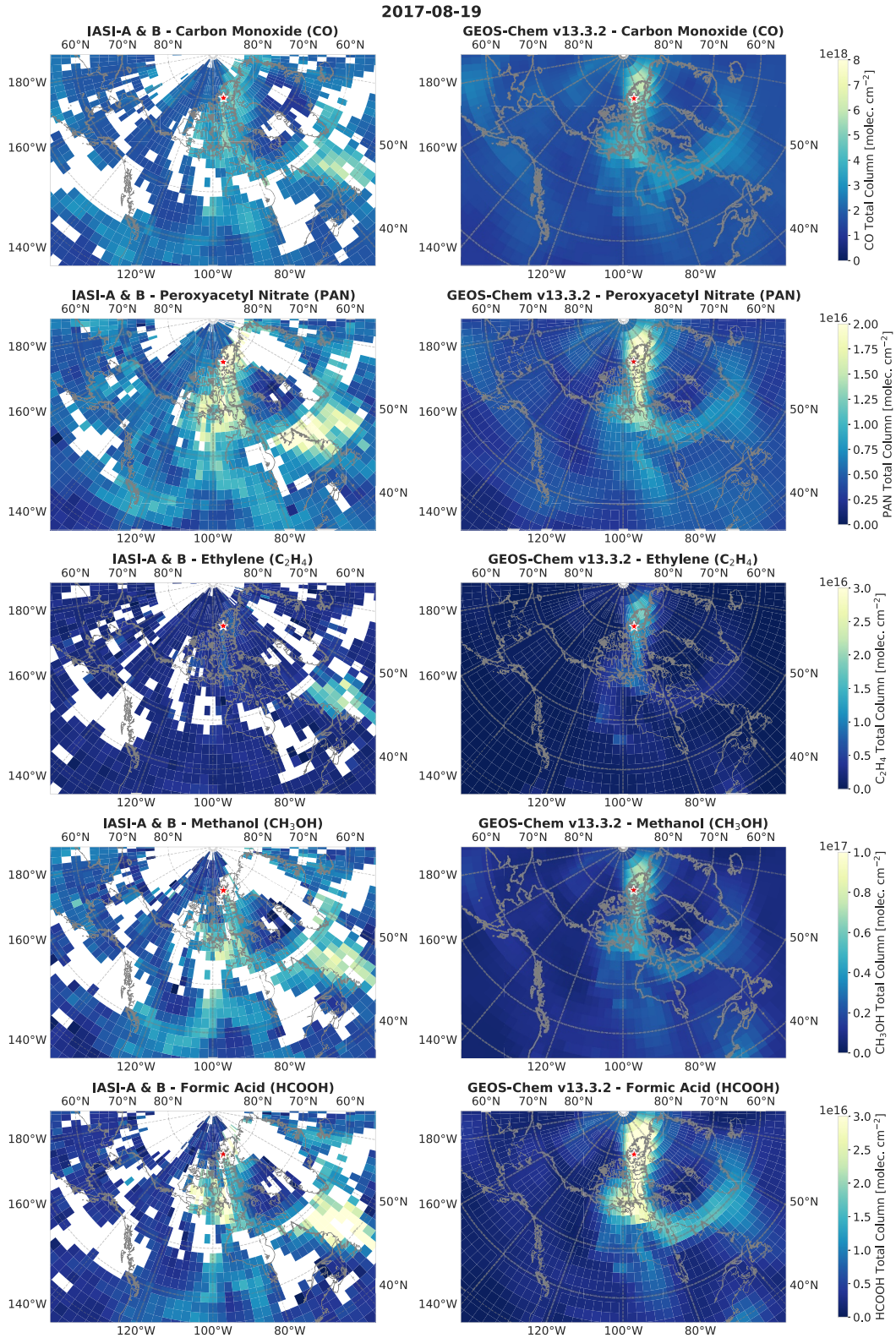

Figure 5. (Left column) Daily averaged IASI-A and IASI-B total columns of CO, PAN, C_2H_4, CH_3OH, and HCOOH on 19 August 2017 re-gridded to the 2° × 2.5° model grid. (Right column) GEOS-Chem total columns of CO, PAN, C_2H_4, CH_3OH, and HCOOH on 19 August 2017 taken from the simulation with modified injection heights for the BC and NWT fires. The location of Eureka is shown by a red star.

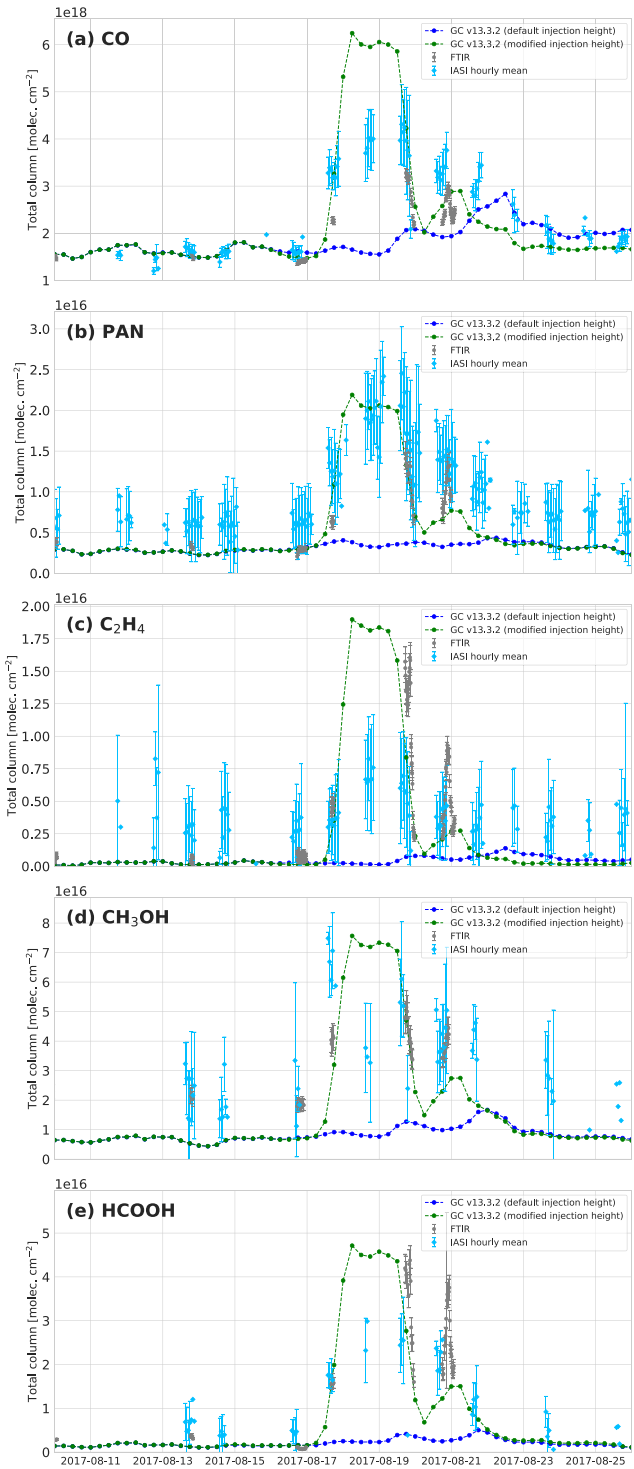

Figure 6. Time-series of un-smoothed GEOS-Chem columns of (a) CO, (b) PAN, (c) C_2H_4, (d) CH_3OH, and (e) HCOOH for the baseline simulation (blue), and the modified injection height simulation (green). PEARL-FTIR measurements are shown in gray, and IASI-A and IASI-B hourly averages within 150 km of Eureka are shown in cyan.

with the PEARL-FTIR on the following day. Between 19 and 21 August, there is general agreement across the PEARL-FTIR and IASI observations, and the simulated GEOS-Chem CO columns. GEOS-Chem PAN columns agree well with the PEARL-FTIR measurements on 19 August, but are biased low relative to the ground-based measurements on 20 and 21 August. A similar pattern to that for PAN between GEOS-Chem and the PEARL-FTIR is seen for C_2H_4, CH_3OH, and HCOOH, which are all biased low in the model on 20 and 21 August. The general agreement between the GEOS-Chem simulated columns and the PEARL-FTIR measurements near the peak enhancement on 19 August suggests that the large retrieved columns from the FTIR (particularly for C_2H_4 and HCOOH) are not unrealistic.

Lastly, we investigated the vertical localization of the GEOS-Chem simulated biomass burning plumes in the vicinity of Eureka in the modified injection height simulation. A plot of daily mean GEOS-Chem CO VMR and partial column profiles during the fire period of 17–23 August 2017 are provided as Figure S7 in Supporting Information S1, along with the mean FTIR profiles in the same period. A clear peak representing the biomass burning plume can be seen in the GEOS-Chem CO profiles on 17 and 18 August in the range of 4–6 km, broadly agreeing with location of the peak in the mean retrieved FTIR CO profiles. A study of the 2017 smoke plumes using a ground-based lidar at Eureka and the Navy Aerosol Analysis and Prediction System (NAAPS) model by Ranjbar et al. (2019) found that the BC and NWT plumes were vertically distinct, and that the BC plume was located at an altitude of approximately 7 km above PEARL, while the smoke from the NWT fires was located at an approximate altitude of 4 km. While the model profiles show some layering, the FTIR measurements are not able to vertically resolve the two distinct biomass burning plumes in the profiles, resulting in a single wide peak in the FTIR CO profiles at Eureka. However, the general altitude of the plume is consistent across the PEARL-FTIR and GEOS-Chem profiles in this work, and the findings of Ranjbar et al. (2019).

3.3.2. Estimating Secondary VOC Production

To determine whether the values of our derived emission ratios and emission factors for CH_3OH and HCOOH are being influenced by secondary production of these species as the plume was transported, we use GEOS-Chem to obtain an estimate of fraction of the total columns observed at Eureka that are a result of secondary in-plume production. To accomplish this, we performed a set of independent simulations with the GFAS emissions of each species switched off. We then compare the simulated columns on 18 and 19 August 2017, the days of the peak observed enhancement, with the simulations with the GFAS fire emissions switched on. To negate any influence from ambient column abundances of each species, we calculate the mean pre-fire total columns in the period of 1–15 August 2017, and then subtract this from the fire-affected total columns of each simulation.

The time series of these simulations is shown in Figure 7. For both CH_3OH and HCOOH, the simulations without direct fire emissions lead to a significant decrease in the resulting columns at Eureka on 18 and 19 August. For CH_3OH, there is a very small enhancement, and the mean peak columns in the no-emission simulation are approximately 3% of the those in the simulation with direct fire emissions, suggesting a very small in-plume secondary production component. This indicates that the derived emission ratio and emission factor for CH_3OH is likely not overestimated due to secondary production. For HCOOH in the no-emissions scenario, there is still a notable

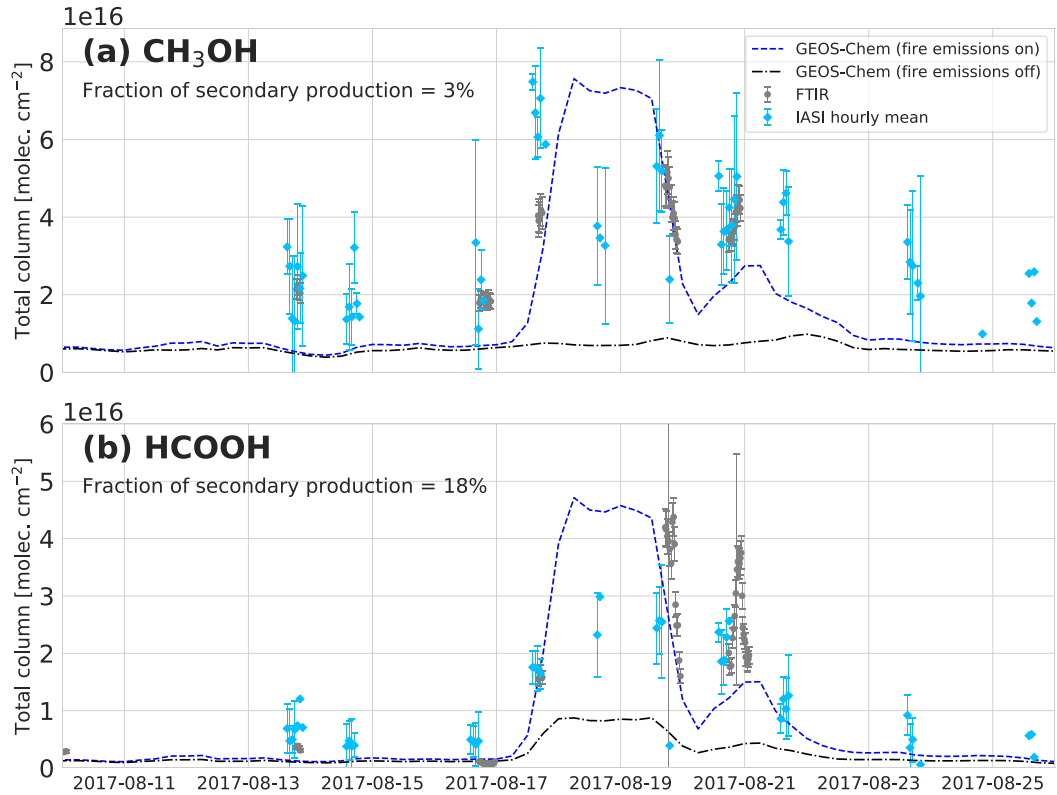

Figure 7. Time-series of un-smoothed GEOS-Chem columns of (a) CH_3OH, and (b) HCOOH for the modified injection height simulation (blue dashed line), and simulations where direct GFAS fire emissions of each species were turned off (black dashed line). The fraction of secondary production was determined as the mean relative difference (i.e., $100 \times \frac{x_{on} - x_{off}}{x_{on}}$) between the two simulations during the peak enhancement on 18 and 19 August, after correcting for the background pre-fire column abundances.

enhancement at Eureka that is approximately 18% of the peak columns in the original simulation, indicating that there is a non-negligible secondary in-plume production component in the resulting enhancement at Eureka. This finding is consistent with a recent study by Chen et al. (2021) who used airborne measurements from the Atmospheric Tomography (ATom) missions and GEOS-Chem to highlight a significant secondary production component of HCOOH in aged biomass burning plumes, leading to CO:HCOOH enhancement ratios that broadly increase with plume age. It should be noted, however, that due to the effects of numerical diffusion on transported plumes in global Eulerian models (Eastham & Jacob, 2017) and the fact that precursor species within these plumes are diluted over the model grid-boxes, these estimates of secondary production should likely be viewed as a lower limit. In addition, missing chemical pathways in the model could contribute to discrepancies in the model simulation. Reducing the HCOOH emission factors from the PEARL-FTIR and IASI by 18% to account for this secondary production, we arrive at values of 11.69 ± 4.78 g kg^{-1} and 4.56 ± 2.06 g kg^{-1}, respectively. These corrected emission factors are still significantly larger than the values provided in all previous studies, suggesting that the emissions of HCOOH from the NWT and BC fires were much larger than previously reported.

4. Conclusions

The August 2017 BCE and NWT wildfires led to the largest observed short-term perturbations in the budgets of PAN, C_2H_4, and HCOOH in the 2006–2020 time-series of measurements by the PEARL-FTIR at Eureka. In general, IASI observed a similar temporal pattern in the enhancements but smaller columns of most species in comparison to the PEARL-FTIR, which can likely be attributed to the reduced sensitivity of the IASI retrievals at high latitudes as a result of low thermal contrast in the region. We have derived enhancement and emission ratios, as well as emission factors for all species relative to CO from both PEARL-FTIR and IASI measurements.

The derived emission factors for PAN and CH_3OH are in good agreement between the PEARL-FTIR, IASI and previous studies, while those for C_2H_4 and HCOOH, particularly those from the PEARL-FTIR, are significantly larger than previously reported in the literature.

The GEOS-Chem CTM was used to simulate the transport of the wildfire plumes and the subsequent enhancements of each species at Eureka. Using the default biomass burning injection scheme of GFAS in the model produces a severe transport error leading to unrealistically small enhancements, and poor correlations with PEARL-FTIR and IASI measurements in the vicinity of Eureka. By modifying the injection height scheme, and injecting the emissions directly at higher model levels, GEOS-Chem reproduces the transport and the observed enhancements much more accurately. Using CO and PAN as tracer species for the fire plumes, we performed model sensitivity tests to determine the appropriate injection heights for fires, finding that injection heights of 12.5 km for the BC fires, based on Fromm et al. (2021) and Peterson et al. (2018), and 10 km for the NWT fires, produced the strongest correlations with ground-based FTIR observations at Eureka for CO and PAN. Lastly, we used GEOS-Chem to approximate the portions of the observed total columns at Eureka which resulted from secondary in-plume production. It was found that for CH_3OH, there was minimal secondary production (approximately 3% of the observed total columns). However, for HCOOH, secondary production was a more significant component (approximately 18%) of the peak observed columns at Eureka. After applying a correction to the calculated HCOOH emission factors from the PEARL-FTIR and IASI, there is still a significant discrepancy with the values previously reported in the literature, which suggests unusually large HCOOH emissions from the August 2017 fires.

In general, the August 2017 wildfires were a major biomass burning event, one that demonstrates how resulting biomass burning plumes can lead to significant transient perturbations far above baseline concentrations of short-lived VOCs in the high Arctic. It is expected that as wildfires increase in frequency and severity due to anthropogenic climate change, events such as these will continue to occur and may grow in magnitude and scale. Biomass burning is expected to become an increasingly large component of the budgets and annual cycles of reactive VOCs at high latitudes; the climatic and environmental impacts of these VOCs on the highly sensitive Arctic region thus deserve further investigation.

Data Availability Statement

Version 13.3.2 of the GEOS-Chem model (GEOS-Chem, 2021) was used in this work, and is freely available to the public via https://doi.org/10.5281/zenodo.5711194. Instructions for downloading and running the model can be found online (https://geos-chem.readthedocs.io/). A description of the model and configuration used in this study is provided in the text. The authors acknowledge the use of the GFASv1.2 emissions inventory, which contains modified Copernicus Atmosphere Monitoring Service information (2018). B. Franco and L. Clarisse provided the IASI CO, PAN, C_2H_4, CH_3OH, and HCOOH products for the purposes of this study. The 2006–2020 Eureka FTIR CO, PAN, C_2H_4, CH_3OH, and HCOOH products, the IASI dataset used in this study, and the modified GFAS files used for the GEOS-Chem simulations are available on the Borealis Canadian Dataverse Repository (Wizenberg et al., 2022) which is accessible at https://doi.org/10.5683/SP3/6PBAHK.

Acknowledgments
Bruker FTIR measurements were made at PEARL by the Canadian Network for the Detection of Atmospheric Composition Change (CANDAC), which has been supported by the Atlantic Innovation Fund/Nova Scotia Research Innovation Trust, Canada Foundation for Innovation, Canadian Foundation for Climate and Atmospheric Sciences, Canadian Space Agency (CSA), Environment and Climate Change Canada (ECCC), Government of Canada International Polar Year funding, Natural Sciences and Engineering Research Council (NSERC), Northern Scientific Training Program, Ontario Innovation Trust, Polar Continental Shelf Program, and Ontario Research Fund. We thank former CANDAC/PEARL/PAHA PI James Drummond, Canadian Arctic ACE/OSIRIS Validation Campaign PI Kaley Walker, PEARL Site Manager Pierre Fogal, CANDAC Data Manager Yan Tsehtik, the CANDAC operators, and the staff at ECCCs Eureka Weather Station for their contributions to data acquisition, and for logistical and on-site support. We thank Dr G. C. Toon (Jet Propulsion Laboratory, California Institute of Technology, Pasadena, CA) for generating and making available the pseudo-linelists as well as the ATM20 line-by-line compilation. The MERRA-2 and GEOS-FP meteorological fields used in the GEOS-Chem simulations in this work were provided by NASA/GMAO. IASI is a joint mission of EUMETSAT and the Centre National d'Etudes Spatiales (CNES, France). The authors acknowledge the AERIS data infrastructure for providing access to the IASI data, Daniel Hurtmans for the development of the CO retrievals, and EUMETSAT AC SAF for CO data production. The research at ULB has been supported by the IASI.Flow Prodex arrangement (ESA–BELSPO). Lieven Clarisse is a research associate supported by the F.R.S.–FNRS. E. Mahieu is a senior research associate supported by the Belgian F.R.S.–FNRS.

References

Akagi, S. K., Yokelson, R. J., Burling, I. R., Meinardi, S., Simpson, I., Blake, D. R., et al. (2013). Measurements of reactive trace gases and variable O_3 formation rates in some South Carolina biomass burning plumes. *Atmospheric Chemistry and Physics*, *13*(3), 1141–1165. https://doi.org/10.5194/acp-13-1141-2013

Akagi, S. K., Yokelson, R. J., Wiedinmyer, C., Alvarado, M. J., Reid, J. S., Karl, T., et al. (2011). Emission factors for open and domestic biomass burning for use in atmospheric models. *Atmospheric Chemistry and Physics*, *11*(9), 4039–4072. https://doi.org/10.5194/acp-11-4039-2011

Alvarado, M. J., Cady-Pereira, K. E., Xiao, Y., Millet, D. B., & Payne, V. H. (2011). Emission ratios for ammonia and formic acid and observations of peroxy acetyl nitrate (PAN) and ethylene in biomass burning smoke as seen by the Tropospheric Emission Spectrometer (TES). *Atmosphere*, *2*(4), 633–654. https://doi.org/10.3390/atmos2040633

Alvarado, M. J., Logan, J. A., Mao, J., Apel, E., Riemer, D., Blake, D., et al. (2010). Nitrogen oxides and PAN in plumes from boreal fires during ARCTAS-B and their impact on ozone: An integrated analysis of aircraft and satellite observations. *Atmospheric Chemistry and Physics*, *10*(20), 9739–9760. https://doi.org/10.5194/acp-10-9739-2010

Andreae, M. O. (2019). Emission of trace gases and aerosols from biomass burning – An updated assessment. *Atmospheric Chemistry and Physics*, *19*(13), 8523–8546. https://doi.org/10.5194/acp-19-8523-2019

Andreae, M. O., & Merlet, P. (2001). Emission of trace gases and aerosols from biomass burning. *Global Biogeochemical Cycles*, *15*(4), 955–966. https://doi.org/10.1029/2000gb001382

Ashworth, K., Chung, S. H., McKinney, K. A., Liu, Y., Munger, J. W., Martin, S. T., & Steiner, A. L. (2016). Modelling bidirectional fluxes of methanol and acetaldehyde with the FORCAsT canopy exchange model. *Atmospheric Chemistry and Physics*, *16*(24), 15461–15484. https://doi.org/10.5194/acp-16-15461-2016

Bader, W., Stavrakou, T., Muller, J.-F., Reimann, S., Boone, C. D., Harrison, J. J., et al. (2014). Long-term evolution and seasonal modulation of methanol above Jungfraujoch (46.5° N, 8.0° E): Optimisation of the retrieval strategy, comparison with model simulations and independent observations. *Atmospheric Measurement Techniques*, *7*(11), 3861–3872. https://doi.org/10.5194/amt-7-3861-2014

Batchelor, R. L., Strong, K., Lindenmaier, R., Mittermeier, R. L., Fast, H., Drummond, J. R., & Fogal, P. F. (2009). A new Bruker IFS 125HR FTIR spectrometer for the Polar Environment Atmospheric Research Laboratory at Eureka, Nunavut, Canada: Measurements and comparison with the existing Bomem DA8 spectrometer. *Journal of Atmospheric and Oceanic Technology*, *26*(7), 1328–1340. https://doi.org/10.1175/2009jtecha1215.1

Bates, K. H., Jacob, D. J., Wang, S., Hornbrook, R. S., Apel, E. C., Kim, M. J., et al. (2021). The global budget of atmospheric methanol: New constraints on secondary, oceanic, and terrestrial sources. *Journal of Geophysical Research: Atmospheres*, *126*(4), e2020JD033439. https://doi.org/10.1029/2020jd033439

BC Wildfire Service. (2017). *Wildfire season summary*. Province of British Columbia. Retrieved from https://www2.gov.bc.ca/gov/content/safety/wildfire-status/about-bcws/wildfire-history/wildfire-season-summary

Beine, H. J., & Krognes, T. (2000). The seasonal cycle of peroxyacetyl nitrate (PAN) in the European Arctic. *Atmospheric Environment*, *34*(6), 933–940. https://doi.org/10.1016/s1352-2310(99)00288-5

Bey, I., Jacob, D. J., Yantosca, R. M., Logan, J. A., Field, B. D., Fiore, A. M., et al. (2001). Global modeling of tropospheric chemistry with assimilated meteorology: Model description and evaluation. *Journal of Geophysical Research*, *106*(D19), 23073–23095. https://doi.org/10.1029/2001jd000807

Bourassa, A. E., Rieger, L. A., Zawada, D. J., Khaykin, S., Thomason, L. W., & Degenstein, D. A. (2019). Satellite limb observations of unprecedented forest fire aerosol in the stratosphere. *Journal of Geophysical Research: Atmospheres*, *124*(16), 9510–9519. https://doi.org/10.1029/2019jd030607

Bridier, I., Caralp, F., Loirat, H., Lesclaux, R., Veyret, B., Becker, K. H., et al. (1991). Kinetic and theoretical studies of the reactions acetylperoxy + nitrogen dioxide + M ⇌ acetyl peroxynitrate + M between 248 and 393 K and between 30 and 760 Torr. *The Journal of Physical Chemistry*, *95*(9), 3594–3600. https://doi.org/10.1021/j100162a031

Cady-Pereira, K. E., Chaliyakunnel, S., Shephard, M. W., Millet, D. B., Luo, M., & Wells, K. C. (2014). HCOOH measurements from space: TES retrieval algorithm and observed global distribution. *Atmospheric Measurement Techniques*, *7*(7), 2297–2311. https://doi.org/10.5194/amt-7-2297-2014

Cady-Pereira, K. E., Shephard, M. W., Millet, D. B., Luo, M., Wells, K. C., Xiao, Y., et al. (2012). Methanol from TES global observations: Retrieval algorithm and seasonal and spatial variability. *Atmospheric Chemistry and Physics*, *12*(17), 8189–8203. https://doi.org/10.5194/acp-12-8189-2012

Chameides, W. L., & Davis, D. D. (1983). Aqueous-phase source of formic acid in clouds. *Nature*, *304*(5925), 427–429. https://doi.org/10.1038/304427a0

Chen, X., Millet, D. B., Neuman, J. A., Veres, P. R., Ray, E. A., Commane, R., et al. (2021). HCOOH in the remote atmosphere: Constraints from Atmospheric Tomography (ATom) airborne observations. *ACS Earth and Space Chemistry*, *5*(6), 1436–1454. https://doi.org/10.1021/acsearthspacechem.1c00049

Chen, X., Millet, D. B., Singh, H. B., Wisthaler, A., Apel, E. C., Atlas, E. L., et al. (2019). On the sources and sinks of atmospheric VOCs: An integrated analysis of recent aircraft campaigns over North America. *Atmospheric Chemistry and Physics*, *19*(14), 9097–9123. https://doi.org/10.5194/acp-19-9097-2019

Clerbaux, C., Boynard, A., Clarisse, L., George, M., Hadji-Lazaro, J., Herbin, H., et al. (2009). Monitoring of atmospheric composition using the thermal infrared IASI/MetOp sounder. *Atmospheric Chemistry and Physics*, *9*(16), 6041–6054. https://doi.org/10.5194/acp-9-6041-2009

Coheur, P.-F., Clarisse, L., Turquety, S., Hurtmans, D., & Clerbaux, C. (2009). IASI measurements of reactive trace species in biomass burning plumes. *Atmospheric Chemistry and Physics*, *9*(15), 5655–5667. https://doi.org/10.5194/acp-9-5655-2009

Coheur, P.-F., Herbin, H., Clerbaux, C., Hurtmans, D., Wespes, C., Carleer, M., et al. (2007). ACE-FTS observation of a young biomass burning plume: First reported measurements of C_2H_4, C_3H_6O, H_2CO, and PAN by infrared occultation from space. *Atmospheric Chemistry and Physics*, *7*(20), 5437–5446. https://doi.org/10.5194/acp-7-5437-2007

Dolan, W., Payne, V. H., Kualwik, S. S., & Bowman, K. W. (2016). Satellite observations of ethylene (C_2H_4) from the Aura Tropospheric Emission Spectrometer: A scoping study. *Atmospheric Environment*, *141*, 388–393. https://doi.org/10.1016/j.atmosenv.2016.07.009

Dufour, G., Boone, C. D., Rinsland, C. P., & Bernath, P. F. (2006). First space-borne measurements of methanol inside aged southern tropical to mid-latitude biomass burning plumes using the ACE-FTS instrument. *Atmospheric Chemistry and Physics*, *6*(11), 3463–3470. https://doi.org/10.5194/acp-6-3463-2006

Dufour, G., Szopa, S., Hauglustaine, D. A., Boone, C. D., Rinsland, C. P., & Bernath, P. F. (2007). The influence of biogenic emissions on upper-tropospheric methanol as revealed from space. *Atmospheric Chemistry and Physics*, *7*(24), 6119–6129. https://doi.org/10.5194/acp-7-6119-2007

Eastham, S. D., & Jacob, D. J. (2017). Limits on the ability of global Eulerian models to resolve intercontinental transport of chemical plumes. *Atmospheric Chemistry and Physics*, *17*(4), 2543–2553. https://doi.org/10.5194/acp-17-2543-2017

Fall, R., & Benson, A. A. (1996). Leaf methanol — The simplest natural product from plants. *Trends in Plant Science*, *1*(9), 296–301. https://doi.org/10.1016/s1360-1385(96)88175-0

Fischer, E. V., Jacob, D. J., Yantosca, R. M., Sulprizio, M. P., Millet, D. B., Mao, J., et al. (2014). Atmospheric peroxyacetyl nitrate (PAN): A global budget and source attribution. *Atmospheric Chemistry and Physics*, *14*(5), 2679–2698. https://doi.org/10.5194/acp-14-2679-2014

Fischer, E. V., Jaffe, D. A., & Weatherhead, E. C. (2011). Free tropospheric peroxyacetyl nitrate (PAN) and ozone at Mount Bachelor: Potential causes of variability and timescale for trend detection. *Atmospheric Chemistry and Physics*, *11*(12), 5641–5654. https://doi.org/10.5194/acp-11-5641-2011

Flannigan, M. D., Logan, K. A., Amiro, B. D., Skinner, W. R., & Stocks, B. J. (2005). Future area burned in Canada. *Climatic Change*, *72*(1–2), 1–16. https://doi.org/10.1007/s10584-005-5935-y

Folberth, G. A., Hauglustaine, D. A., Lathière, J., & Brocheton, F. (2006). Interactive chemistry in the Laboratoire de Météorologie Dynamique General Circulation Model: Model description and impact analysis of biogenic hydrocarbons on tropospheric chemistry. *Atmospheric Chemistry and Physics*, *6*(8), 2273–2319. https://doi.org/10.5194/acp-6-2273-2006

Franco, B., Blumenstock, T., Cho, C., Clarisse, L., Clerbaux, C., Coheur, P.-F., et al. (2021). Ubiquitous atmospheric production of organic acids mediated by cloud droplets. *Nature*, *593*(7858), 233–237. https://doi.org/10.1038/s41586-021-03462-x

Franco, B., Clarisse, L., Stavrakou, T., Müller, J., Taraborrelli, D., Hadji-Lazaro, J., et al. (2020). Spaceborne measurements of formic and acetic acids: A global view of the regional sources. *Geophysical Research Letters*, *47*(4), e2019GL086239. https://doi.org/10.1029/2019gl086239

Franco, B., Clarisse, L., Stavrakou, T., Müller, J., Van Damme, M., Whitburn, S., et al. (2018). A general framework for global retrievals of trace gases from IASI: Application to methanol, formic acid, and PAN. *Journal of Geophysical Research: Atmospheres*, *123*(24), 13,963–13,984. https://doi.org/10.1029/2018jd029633

Franco, B., Clarisse, L., Van Damme, M., Hadji-Lazaro, J., Clerbaux, C., & Coheur, P.-F. (2022). Ethylene industrial emitters seen from space. *Nature Communications*, *13*(1), 6452. https://doi.org/10.1038/s41467-022-34098-8

Freitas, S. R., Longo, K. M., & Andreae, M. O. (2006). Impact of including the plume rise of vegetation fires in numerical simulations of associated atmospheric pollutants. *Geophysical Research Letters*, *33*(17), L17808. https://doi.org/10.1029/2006gl026608

Fromm, M. D., Kablick, G. P., Peterson, D. A., Kahn, R. A., Flower, V. J., & Seftor, C. J. (2021). Quantifying the source term and uniqueness of the august 12, 2017 Pacific Northwest pyrocb event. *Journal of Geophysical Research: Atmospheres*, *126*(13), e2021JD034928. https://doi.org/10.1029/2021jd034928

Galloway, J. N., Likens, G. E., Keene, W. C., & Miller, J. M. (1982). The composition of precipitation in remote areas of the world. *Journal of Geophysical Research*, *87*(C11), 8771. https://doi.org/10.1029/jc087ic11p08771

Gatz, D. F., & Smith, L. (1995). The standard error of a weighted mean concentration—II. Estimating confidence intervals. *Atmospheric Environment*, *29*(11), 1195–1200. https://doi.org/10.1016/1352-2310(94)00209-4

Gelaro, R., McCarty, W., Suárez, M. J., Todling, R., Molod, A., Takacs, L., et al. (2017). The modern-era retrospective analysis for research and applications, Version 2 (MERRA-2). *Journal of Climate*, *30*(14), 5419–5454. https://doi.org/10.1175/jcli-d-16-0758.1

Gentner, D. R., Worton, D. R., Isaacman, G., Davis, L. C., Dallmann, T. R., Wood, E. C., et al. (2013). Chemical composition of gas-phase organic carbon emissions from motor vehicles and implications for ozone production. *Environmental Science & Technology*, *47*(20), 11837–11848. https://doi.org/10.1021/es401470e

George, M., Clerbaux, C., Bouarar, I., Coheur, P.-F., Deeter, M. N., Edwards, D. P., et al. (2015). An examination of the long-term CO records from MOPITT and IASI: Comparison of retrieval methodology. *Atmospheric Measurement Techniques*, *8*(10), 4313–4328. https://doi.org/10.5194/amt-8-4313-2015

GEOS-Chem. (2021). GEOS-Chem classic (Version 13.3.2) [Software]. Zenodo. https://doi.org/10.5281/zenodo.5711194

González Abad, G., Bernath, P. F., Boone, C. D., McLeod, S. D., Manney, G. L., & Toon, G. C. (2009). Global distribution of upper tropospheric formic acid from the ACE-FTS. *Atmospheric Chemistry and Physics*, *9*(20), 8039–8047. https://doi.org/10.5194/acp-9-8039-2009

Goode, J. G., Yokelson, R. J., Ward, D. E., Susott, R. A., Babbitt, R. E., Davies, M. A., & Hao, W. M. (2000). Measurements of excess O_3, CO_2, CO, CH_4, C_2H_4, C_2H_2, HCN, NO, NH_3, HCOOH, CH_3COOH, HCHO, and CH_3OH in 1997 Alaskan biomass burning plumes by airborne Fourier transform infrared spectroscopy (AFTIR). *Journal of Geophysical Research*, *105*(D17), 22147–22166. https://doi.org/10.1029/2000jd900287

Gordon, I., Rothman, L., Hill, C., Kochanov, R., Tan, Y., Bernath, P., et al. (2017). The HITRAN2016 molecular spectroscopic database. *Journal of Quantitative Spectroscopy and Radiative Transfer*, *203*, 3–69. https://doi.org/10.1016/j.jqsrt.2017.06.038

Guenther, A. B., Jiang, X., Heald, C. L., Sakulyanontvittaya, T., Duhl, T., Emmons, L. K., & Wang, X. (2012). The model of emissions of gases and aerosols from nature Version 2.1 (MEGAN2.1): An extended and updated framework for modeling biogenic emissions. *Geoscientific Model Development*, *5*(6), 1471–1492. https://doi.org/10.5194/gmd-5-1471-2012

Halofsky, J. E., Peterson, D. L., & Harvey, B. J. (2020). Changing wildfire, changing forests: The effects of climate change on fire regimes and vegetation in the Pacific Northwest, USA. *Fire Ecology*, *16*(1), 4. https://doi.org/10.1186/s42408-019-0062-8

Herbin, H., Hurtmans, D., Clarisse, L., Turquety, S., Clerbaux, C., Rinsland, C. P., et al. (2009). Distributions and seasonal variations of tropospheric ethene (C_2H_4) from Atmospheric Chemistry Experiment (ACE-FTS) solar occultation spectra. *Geophysical Research Letters*, *36*(4), L04801. https://doi.org/10.1029/2008gl036338

Hoesly, R. M., Smith, S. J., Feng, L., Klimont, Z., Janssens-Maenhout, G., Pitkanen, T., et al. (2018). Historical (1750–2014) anthropogenic emissions of reactive gases and aerosols from the Community Emissions Data System (CEDS). *Geoscientific Model Development*, *11*(1), 369–408. https://doi.org/10.5194/gmd-11-369-2018

Holloway, T., Levy, H., & Kasibhatla, P. (2000). Global distribution of carbon monoxide. *Journal of Geophysical Research*, *105*(D10), 12123–12147. https://doi.org/10.1029/1999jd901173

Hope, E. S., McKenney, D. W., Pedlar, J. H., Stocks, B. J., & Gauthier, S. (2016). Wildfire suppression costs for Canada under a changing climate. *PLoS One*, *11*(8), e0157425. https://doi.org/10.1371/journal.pone.0157425

Horowitz, L. W., Walters, S., Mauzerall, D. L., Emmons, L. K., Rasch, P. J., Granier, C., et al. (2003). A global simulation of tropospheric ozone and related tracers: Description and evaluation of MOZART, version 2. *Journal of Geophysical Research*, *108*(D24), 4784. https://doi.org/10.1029/2002jd002853

Hurtmans, D., Coheur, P.-F., Wespes, C., Clarisse, L., Scharf, O., Clerbaux, C., et al. (2012). FORLI radiative transfer and retrieval code for IASI. *Journal of Quantitative Spectroscopy and Radiative Transfer*, *113*(11), 1391–1408. https://doi.org/10.1016/j.jqsrt.2012.02.036

Hüve, K., Christ, M., Kleist, E., Uerlings, R., Niinemets, U., Walter, A., & Wildt, J. (2007). Simultaneous growth and emission measurements demonstrate an interactive control of methanol release by leaf expansion and stomata. *Journal of Experimental Botany*, *58*(7), 1783–1793. https://doi.org/10.1093/jxb/erm038

Jacob, D. (2000). Heterogeneous chemistry and tropospheric ozone. *Atmospheric Environment*, *34*(12–14), 2131–2159. https://doi.org/10.1016/s1352-2310(99)00462-8

Jacob, D. J. (1986). Chemistry of OH in remote clouds and its role in the production of formic acid and peroxymonosulfate. *Journal of Geophysical Research*, *91*(D9), 9807. https://doi.org/10.1029/jd091id09p09807

Juncosa Calahorrano, J. F., Lindaas, J., O'Dell, K., Palm, B. B., Peng, Q., Flocke, F., et al. (2020). Daytime oxidized reactive nitrogen partitioning in western U.S. wildfire smoke plumes. *Journal of Geophysical Research: Atmospheres*, *126*(4), e2020JD033484. https://doi.org/10.1029/2020jd033484

Juncosa Calahorrano, J. F., Payne, V. H., Kulawik, S., Ford, B., Flocke, F., Campos, T., & Fischer, E. V. (2021). Evolution of acyl peroxynitrates (PANs) in wildfire smoke plumes detected by the Cross-Track Infrared Sounder (CrIS) over the western U.S. during summer 2018. *Geophysical Research Letters*, *48*(23), e2021gl093405. https://doi.org/10.1029/2021gl093405

Kaiser, J. W., Heil, A., Andreae, M. O., Benedetti, A., Chubarova, N., Jones, L., et al. (2012). Biomass burning emissions estimated with a global fire assimilation system based on observed fire radiative power. *Biogeosciences*, *9*(1), 527–554. https://doi.org/10.5194/bg-9-527-2012

Kasibhatla, P. S., Levy, H., & Moxim, W. J. (1993). Global NO_x, HNO_3, PAN, and NO_y distributions from fossil fuel combustion emissions: A model study. *Journal of Geophysical Research*, *98*(D4), 7165–7180. https://doi.org/10.1029/92jd02845

Keene, W. C., Galloway, J. N., Likens, G. E., Deviney, F. A., Mikkelsen, K. N., Moody, J. L., & Maben, J. R. (2015). Atmospheric wet deposition in remote regions: Benchmarks for environmental change. *Journal of the Atmospheric Sciences*, *72*(8), 2947–2978. https://doi.org/10.1175/jas-d-14-0378.1

Kerzenmacher, T., Dils, B., Kumps, N., Blumenstock, T., Clerbaux, C., Coheur, P.-F., et al. (2012). Validation of IASI FORLI carbon monoxide retrievals using FTIR data from NDACC. *Atmospheric Measurement Techniques*, *5*(11), 2751–2761. https://doi.org/10.5194/amt-5-2751-2012

Khaykin, S. M., Godin-Beekmann, S., Hauchecorne, A., Pelon, J., Ravetta, F., & Keckhut, P. (2018). Stratospheric smoke with unprecedentedly high backscatter observed by lidars above southern France. *Geophysical Research Letters*, *45*(3), 1639–1646. https://doi.org/10.1002/2017gl076763

Kirchmeier-Young, M. C., Gillett, N. P., Zwiers, F. W., Cannon, A. J., & Anslow, F. S. (2019). Attribution of the influence of human-induced climate change on an extreme fire season. *Earth's Future*, *7*(1), 2–10. https://doi.org/10.1029/2018ef001050

Kloss, C., Berthet, G., Sellitto, P., Ploeger, F., Bucci, S., Khaykin, S., et al. (2019). Transport of the 2017 Canadian wildfire plume to the tropics via the Asian monsoon circulation. *Atmospheric Chemistry and Physics*, *19*(21), 13547–13567. https://doi.org/10.5194/acp-19-13547-2019

Law, K. S., & Stohl, A. (2007). Arctic air pollution: Origins and impacts. *Science*, *315*(5818), 1537–1540. https://doi.org/10.1126/science.1137695

Law, K. S., Stohl, A., Quinn, P. K., Brock, C. A., Burkhart, J. F., Paris, J.-D., et al. (2014). Arctic air pollution: New insights from POLARCAT-IPY. *Bulletin of the American Meteorological Society*, *95*(12), 1873–1895. https://doi.org/10.1175/bams-d-13-00017.1

Lin, H., Jacob, D. J., Lundgren, E. W., Sulprizio, M. P., Keller, C. A., Fritz, T. M., et al. (2021). Harmonized emissions component (HEMCO) 3.0 as a versatile emissions component for atmospheric models: Application in the GEOS-Chem, NASA GEOS, WRF-GC, CESM2, NOAA GEFS-aerosol, and NOAA UFS models. *Geoscientific Model Development*, *14*(9), 5487–5506. https://doi.org/10.5194/gmd-14-5487-2021

Liu, X., Zhang, Y., Huey, L. G., Yokelson, R. J., Wang, Y., Jimenez, J. L., et al. (2016). Agricultural fires in the south eastern U.S. during SEAC4RS: Emissions of trace gases and particles and evolution of ozone, reactive nitrogen, and organic aerosol. *Journal of Geophysical Research: Atmospheres*, *121*(12), 7383–7414. https://doi.org/10.1002/2016jd025040

Lutsch, E., Dammers, E., Conway, S., & Strong, K. (2016). Long-range transport of NH_3, CO, HCN, and C_2H_6 from the 2014 Canadian wildfires. *Geophysical Research Letters*, *43*(15), 8286–8297. https://doi.org/10.1002/2016gl070114

Lutsch, E., Strong, K., Jones, D. B., Blumenstock, T., Conway, S., Fisher, J. A., et al. (2020). Detection and attribution of wildfire pollution in the Arctic and northern midlatitudes using a network of Fourier-transform infrared spectrometers and GEOS-Chem. *Atmospheric Chemistry and Physics*, *20*(21), 12813–12851. https://doi.org/10.5194/acp-20-12813-2020

Lutsch, E., Strong, K., Jones, D. B., Ortega, I., Hannigan, J. W., Dammers, E., et al. (2019). Unprecedented atmospheric ammonia concentrations detected in the high Arctic from the 2017 Canadian wildfires. *Journal of Geophysical Research: Atmospheres*, *124*(14), 8178–8202. https://doi.org/10.1029/2019jd030419

MacDonald, R. C., & Fall, R. (1993). Detection of substantial emissions of methanol from plants to the atmosphere. *Atmospheric Environment. Part A. General Topics*, *27*(11), 1709–1713. https://doi.org/10.1016/0960-1686(93)90233-o

Mahieu, E., Fischer, E. V., Franco, B., Palm, M., Wizenberg, T., Smale, D., et al. (2021). First retrievals of peroxyacetyl nitrate (PAN) from ground-based FTIR solar spectra recorded at remote sites, comparison with model and satellite data. *Elementa: Science of the Anthropocene*, *9*(1), 00027. https://doi.org/10.1525/elementa.2021.00027

Marsh, D. R., Mills, M. J., Kinnison, D. E., Lamarque, J.-F., Calvo, N., & Polvani, L. M. (2013). Climate change from 1850 to 2005 simulated in CESM1(WACCM). *Journal of Climate*, *26*(19), 7372–7391. https://doi.org/10.1175/jcli-d-12-00558.1

Millet, D. B., Baasandorj, M., Farmer, D. K., Thornton, J. A., Baumann, K., Brophy, P., et al. (2015). A large and ubiquitous source of atmospheric formic acid. *Atmospheric Chemistry and Physics*, *15*(11), 6283–6304. https://doi.org/10.5194/acp-15-6283-2015

Millet, D. B., Jacob, D. J., Custer, T. G., de Gouw, J. A., Goldstein, A. H., Karl, T., et al. (2008). New constraints on terrestrial and oceanic sources of atmospheric methanol. *Atmospheric Chemistry and Physics*, *8*(23), 6887–6905. https://doi.org/10.5194/acp-8-6887-2008

Moxim, W. J., Levy, H., & Kasibhatla, P. S. (1996). Simulated global tropospheric PAN: Its transport and impact on NO_x. *Journal of Geophysical Research*, *101*(D7), 12621–12638. https://doi.org/10.1029/96jd00338

Mungall, E. L., Abbatt, J. P., Wentzell, J. J., Wentworth, G. R., Murphy, J. G., Kunkel, D., et al. (2018). High gas-phase mixing ratios of formic and acetic acid in the high Arctic. *Atmospheric Chemistry and Physics*, *18*(14), 10237–10254. https://doi.org/10.5194/acp-18-10237-2018

Notholt, J., Toon, G., Jones, N., Griffith, D., & Warneke, T. (2006). Spectral line finding program for atmospheric remote sensing using full radiation transfer. *Journal of Quantitative Spectroscopy and Radiative Transfer*, *97*(1), 112–125. https://doi.org/10.1016/j.jqsrt.2004.12.025

Notholt, J., Toon, G. C., Rinsland, C. P., Pougatchev, N. S., Jones, N. B., Connor, B. J., et al. (2000). Latitudinal variations of trace gas concentrations in the free troposphere measured by solar absorption spectroscopy during a ship cruise. *Journal of Geophysical Research*, *105*(D1), 1337–1349. https://doi.org/10.1029/1999jd900940

Olivella, S., & Solé, A. (2004). Unimolecular decomposition of beta-hydroxyethylperoxy radicals in the ho-initiated oxidation of ethene: A theoretical study. *The Journal of Physical Chemistry A*, *108*(52), 11651–11663. https://doi.org/10.1021/jp045944f

Orlando, J. J., Tyndall, G. S., & Calvert, J. G. (1992). Thermal decomposition pathways for peroxyacetyl nitrate (PAN): Implications for atmospheric methyl nitrate levels. *Atmospheric Environment. Part A. General Topics*, *26*(17), 3111–3118. https://doi.org/10.1016/0960-1686(92)90468-z

Paton-Walsh, C., Jones, N. B., Wilson, S. R., Haverd, V., Meier, A., Griffith, D. W., & Rinsland, C. P. (2005). Measurements of trace gas emissions from Australian forest fires and correlations with coincident measurements of aerosol optical depth. *Journal of Geophysical Research*, *110*(D24), D24305. https://doi.org/10.1029/2005jd006202

Paton-Walsh, C., Wilson, S. R., Jones, N. B., & Griffith, D. W. (2008). Measurement of methanol emissions from Australian wildfires by ground-based solar Fourier transform spectroscopy. *Geophysical Research Letters*, *35*(8), L08810. https://doi.org/10.1029/2007gl032951

Paulot, F., Paynter, D., Ginoux, P., Naik, V., Whitburn, S., Van Damme, M., et al. (2017). Gas-aerosol partitioning of ammonia in biomass burning plumes: Implications for the interpretation of spaceborne observations of ammonia and the radiative forcing of ammonium nitrate. *Geophysical Research Letters*, *44*(15), 8084–8093. https://doi.org/10.1002/2017gl074215

Paulot, F., Wunch, D., Crounse, J. D., Toon, G. C., Millet, D. B., DeCarlo, P. F., et al. (2011). Importance of secondary sources in the atmospheric budgets of formic and acetic acids. *Atmospheric Chemistry and Physics*, *11*(5), 1989–2013. https://doi.org/10.5194/acp-11-1989-2011

Payne, V. H., Alvarado, M. J., Cady-Pereira, K. E., Worden, J. R., Kulawik, S. S., & Fischer, E. V. (2014). Satellite observations of peroxyacetyl nitrate from the AURA Tropospheric Emission Spectrometer. *Atmospheric Measurement Techniques*, *7*(11), 3737–3749. https://doi.org/10.5194/amt-7-3737-2014

Payne, V. H., Kulawik, S. S., Fischer, E. V., Brewer, J. F., Huey, L. G., Miyazaki, K., et al. (2022). Satellite measurements of peroxyacetyl nitrate from the cross-track infrared sounder: Comparison with atom aircraft measurements. *Atmospheric Measurement Techniques*, *15*(11), 3497–3511. https://doi.org/10.5194/amt-15-3497-2022

Peterson, D. A., Campbell, J. R., Hyer, E. J., Fromm, M. D., Kablick, G. P., Cossuth, J. H., & DeLand, M. T. (2018). Wildfire-driven thunderstorms cause a volcano-like stratospheric injection of smoke. *NPJ Climate and Atmospheric Science*, *1*(1), 30. https://doi.org/10.1038/s41612-018-0039-3

Peterson, D. A., Fromm, M. D., McRae, R. H., Campbell, J. R., Hyer, E. J., Taha, G., et al. (2021). Australia's black summer pyrocumulonimbus super outbreak reveals potential for increasingly extreme stratospheric smoke events. *NPJ Climate and Atmospheric Science*, *4*(1), 38. https://doi.org/10.1038/s41612-021-00192-9

Philip, S., Martin, R. V., & Keller, C. A. (2016). Sensitivity of chemistry-transport model simulations to the duration of chemical and transport operators: A case study with GEOS-chem V10-01. *Geoscientific Model Development*, *9*(5), 1683–1695. https://doi.org/10.5194/gmd-9-1683-2016

Pommier, M., Clerbaux, C., & Coheur, P.-F. (2017). Determination of enhancement ratios of HCOOH relative to CO in biomass burning plumes by the Infrared Atmospheric Sounding Interferometer (IASI). *Atmospheric Chemistry and Physics*, *17*(18), 11089–11105. https://doi.org/10.5194/acp-17-11089-2017

Pommier, M., Clerbaux, C., Coheur, P.-F., Mahieu, E., Müller, J.-F., Paton-Walsh, C., et al. (2016). HCOOH distributions from IASI for 2008–2014: Comparison with ground-based FTIR measurements and a global chemistry-transport model. *Atmospheric Chemistry and Physics*, *16*(14), 8963–8981. https://doi.org/10.5194/acp-16-8963-2016

Ranjbar, K., O'Neill, N. T., Lutsch, E., McCullough, E. M., AboEl-Fetouh, Y., Xian, P., et al. (2019). Extreme smoke event over the high Arctic. *Atmospheric Environment*, *218*, 117002. https://doi.org/10.1016/j.atmosenv.2019.117002

Razavi, A., Karagulian, F., Clarisse, L., Hurtmans, D., Coheur, P. F., Clerbaux, C., et al. (2011). Global distributions of methanol and formic acid retrieved for the first time from the IASI/MetOp thermal infrared sounder. *Atmospheric Chemistry and Physics*, *11*(2), 857–872. https://doi.org/10.5194/acp-11-857-2011

Rémy, S., Veira, A., Paugam, R., Sofiev, M., Kaiser, J. W., Marenco, F., et al. (2017). Two global data sets of daily fire emission injection heights since 2003. *Atmospheric Chemistry and Physics*, *17*(4), 2921–2942. https://doi.org/10.5194/acp-17-2921-2017

R'Honi, Y., Clarisse, L., Clerbaux, C., Hurtmans, D., Duflot, V., Turquety, S., et al. (2013). Exceptional emissions of NH_3 and HCOOH in the 2010 Russian wildfires. *Atmospheric Chemistry and Physics*, *13*(8), 4171–4181. https://doi.org/10.5194/acp-13-4171-2013

Rinsland, C. P., Dufour, G., Boone, C. D., Bernath, P. F., Chiou, L., Coheur, P.-F., et al. (2007). Satellite boreal measurements over Alaska and Canada during June-July 2004: Simultaneous measurements of upper tropospheric CO, C_2H_6, HCN, CH_3Cl, CH_4, C_2H_2, CH_3OH, HCOOH, OCS, and SF_6 mixing ratios. *Global Biogeochemical Cycles*, *21*(3), GB3008. https://doi.org/10.1029/2006gb002795

Rinsland, C. P., Paton-Walsh, C., Jones, N. B., Griffith, D. W., Goldman, A., Wood, S. W., et al. (2005). High spectral resolution solar absorption measurements of ethylene in a forest fire smoke plume using HITRAN parameters: Tropospheric vertical profile retrieval. *Journal of Quantitative Spectroscopy and Radiative Transfer*, *96*(2), 301–309. https://doi.org/10.1016/j.jqsrt.2005.03.003

Rodgers, C. D. (2000). *Inverse methods for atmospheric sounding: Theory and practice*. World Scientific.

Rodgers, C. D., & Connor, B. J. (2003). Intercomparison of remote sounding instruments. *Journal of Geophysical Research*, *108*(D3), 4116. https://doi.org/10.1029/2002jd002299

Rosanka, S., Franco, B., Clarisse, L., Coheur, P.-F., Pozzer, A., Wahner, A., & Taraborrelli, D. (2021). The impact of organic pollutants from Indonesian peatland fires on the tropospheric and lower stratospheric composition. *Atmospheric Chemistry and Physics*, *21*(14), 11257–11288. https://doi.org/10.5194/acp-21-11257-2021

Rothman, L., Gordon, I., Barbe, A., Benner, D., Bernath, P., Birk, M., et al. (2009). The HITRAN 2008 molecular spectroscopic database. *Journal of Quantitative Spectroscopy and Radiative Transfer*, *110*(9–10), 533–572. https://doi.org/10.1016/j.jqsrt.2009.02.013

Sawada, S., & Totsuka, T. (1986). Natural and anthropogenic sources and fate of atmospheric ethylene. *Atmospheric Environment*, *20*(5), 821–832. https://doi.org/10.1016/0004-6981(86)90266-0

Schobesberger, S., Lopez-Hilfiker, F. D., Taipale, D., Millet, D. B., D'Ambro, E. L., Rantala, P., et al. (2016). High upward fluxes of formic acid from a boreal forest canopy. *Geophysical Research Letters*, *43*(17), 9342–9351. https://doi.org/10.1002/2016gl069599

Simpson, I. J., Akagi, S. K., Barletta, B., Blake, N. J., Choi, Y., Diskin, G. S., et al. (2011). Boreal forest fire emissions in fresh Canadian smoke plumes: C_1-C_{10} volatile organic compounds (VOCs), CO_2, CO, NO_2, NO, HCN, and CH_3CN. *Atmospheric Chemistry and Physics*, *11*(13), 6445–6463. https://doi.org/10.5194/acp-11-6445-2011

Singh, H., Chen, Y., Staudt, A., Jacob, D., Blake, D., Heikes, B., & Snow, J. (2001). Evidence from the Pacific troposphere for large global sources of oxygenated organic compounds. *Nature*, *410*(6832), 1078–1081. https://doi.org/10.1038/35074067

Stanevich, I., Jones, D. B., Strong, K., Parker, R. J., Boesch, H., Wunch, D., et al. (2020). Characterizing model errors in chemical transport modeling of methane: Impact of model resolution in versions V9-02 of GEOS-Chem and V35j of its adjoint model. *Geoscientific Model Development*, *13*(9), 3839–3862. https://doi.org/10.5194/gmd-13-3839-2020

Stavrakou, T., Guenther, A., Razavi, A., Clarisse, L., Clerbaux, C., Coheur, P.-F., et al. (2011). First space-based derivation of the global atmospheric methanol emission fluxes. *Atmospheric Chemistry and Physics*, *11*(10), 4873–4898. https://doi.org/10.5194/acp-11-4873-2011

Stavrakou, T., Müller, J.-F., Peeters, J., Razavi, A., Clarisse, L., Clerbaux, C., et al. (2012). Satellite evidence for a large source of formic acid from boreal and tropical forests. *Nature Geoscience*, *5*(1), 26–30. https://doi.org/10.1038/ngeo1354

Stohl, A. (2006). Characteristics of atmospheric transport into the Arctic troposphere. *Journal of Geophysical Research*, *111*(D11), D11306. https://doi.org/10.1029/2005jd006888

Talukdar, R. K., Burkholder, J. B., Schmoltner, A.-M., Roberts, J. M., Wilson, R. R., & Ravishankara, A. R. (1995). Investigation of the loss processes for peroxyacetyl nitrate in the atmosphere: UV photolysis and reaction with OH. *Journal of Geophysical Research*, *100*(D7), 14163. https://doi.org/10.1029/95jd00545

Tereszchuk, K. A., González Abad, G., Clerbaux, C., Hadji-Lazaro, J., Hurtmans, D., Coheur, P.-F., & Bernath, P. F. (2013). ACE-FTS observations of pyrogenic trace species in boreal biomass burning plumes during BORTAS. *Atmospheric Chemistry and Physics*, *13*(9), 4529–4541. https://doi.org/10.5194/acp-13-4529-2013

Tie, X., Guenther, A., & Holland, E. (2003). Biogenic methanol and its impacts on tropospheric oxidants. *Geophysical Research Letters*, *30*(17), 1881. https://doi.org/10.1029/2003gl017167

Tikhonov, A. N. (1963). On the solution of ill-posed problems and the method of regularization. *Doklady Akademii Nauk*, *151*(3), 501–504.

Toon, G. C. (2022). *Atmospheric Voigt line list for the TCCON 2020 data release*. CaltechDATA. https://doi.org/10.14291/TCCON.GGG2020.ATM.R0. Retrieved from https://data.caltech.edu/records/8972

Toon, G. C., Blavier, J.-F. L., & Sung, K. (2018). Measurements of atmospheric ethene by solar absorption FTIR spectrometry. *Atmospheric Chemistry and Physics*, *18*(7), 5075–5088. https://doi.org/10.5194/acp-18-5075-2018

Torres, O., Bhartia, P. K., Taha, G., Jethva, H., Das, S., Colarco, P., et al. (2020). Stratospheric injection of massive smoke plume from Canadian boreal fires in 2017 as seen by DSCOVR-EPIC, CALIOP, and OMPS-LP observations. *Journal of Geophysical Research: Atmospheres*, *125*(10), e2020JD032579. https://doi.org/10.1029/2020jd032579

Tuazon, E. C., Carter, W. P., & Atkinson, R. (1991). Thermal decomposition of peroxyacetyl nitrate and reactions of acetyl peroxy radicals with nitric oxide and nitrogen dioxide over the temperature range 283-313 K. *The Journal of Physical Chemistry*, *95*(6), 2434–2437. https://doi.org/10.1021/j100159a059

Vander Auwera, J., Fayt, A., Tudorie, M., Rotger, M., Boudon, V., Franco, B., & Mahieu, E. (2014). Self-broadening coefficients and improved line intensities for the ν_7 band of ethylene near 10.5 μm, and impact on ethylene retrievals from Jungfraujoch solar spectra. *Journal of Quantitative Spectroscopy and Radiative Transfer*, *148*, 177–185. https://doi.org/10.1016/j.jqsrt.2014.07.003

Viatte, C., Strong, K., Hannigan, J., Nussbaumer, E., Emmons, L. K., Conway, S., et al. (2015). Identifying fire plumes in the Arctic with tropospheric FTIR measurements and transport models. *Atmospheric Chemistry and Physics*, *15*(5), 2227–2246. https://doi.org/10.5194/acp-15-2227-2015

Viatte, C., Strong, K., Paton-Walsh, C., Mendonca, J., O'Neill, N. T., & Drummond, J. R. (2013). Measurements of CO, HCN, and C_2H_6 total columns in smoke plumes transported from the 2010 Russian boreal forest fires to the Canadian high Arctic. *Atmosphere-Ocean*, *51*(5), 522–531. https://doi.org/10.1080/07055900.2013.823373

Viatte, C., Strong, K., Walker, K. A., & Drummond, J. R. (2014). Five years of CO, HCN, C_2H_6, C_2H_2, CH_3OH, HCOOH, and H_2CO total columns measured in the Canadian high Arctic. *Atmospheric Measurement Techniques*, *7*(6), 1547–1570. https://doi.org/10.5194/amt-7-1547-2014

Vigouroux, C., Stavrakou, T., Whaley, C., Dils, B., Duflot, V., Hermans, C., et al. (2012). FTIR time-series of biomass burning products (HCN, C_2H_6, C_2H_2, CH_3OH, and HCOOH) at Reunion Island (21° S, 55° E) and comparisons with model data. *Atmospheric Chemistry and Physics*, *12*(21), 10367–10385. https://doi.org/10.5194/acp-12-10367-2012

Wang, Y., Logan, J. A., & Jacob, D. J. (1998). Global simulation of tropospheric O_3-NO_x-hydrocarbon chemistry: 2. Model evaluation and global ozone budget. *Journal of Geophysical Research*, *103*(D9), 10727–10755. https://doi.org/10.1029/98jd00157

Wells, K. C., Millet, D. B., Cady-Pereira, K. E., Shephard, M. W., Henze, D. K., Bousserez, N., et al. (2014). Quantifying global terrestrial methanol emissions using observations from the TES satellite sensor. *Atmospheric Chemistry and Physics*, *14*(5), 2555–2570. https://doi.org/10.5194/acp-14-2555-2014

Whitburn, S., Van Damme, M., Clarisse, L., Hurtmans, D., Clerbaux, C., & Coheur, P.-F. (2017). IASI-derived NH_3 enhancement ratios relative to CO for the tropical biomass burning regions. *Atmospheric Chemistry and Physics*, *17*(19), 12239–12252. https://doi.org/10.5194/acp-17-12239-2017

Whitburn, S., Van Damme, M., Clarisse, L., Turquety, S., Clerbaux, C., & Coheur, P.-F. (2016). Doubling of annual ammonia emissions from the peat fires in Indonesia during the 2015 El Niño. *Geophysical Research Letters*, *43*(20), 11007–11014. https://doi.org/10.1002/2016gl070620

Whitburn, S., Van Damme, M., Kaiser, J., van der Werf, G., Turquety, S., Hurtmans, D., et al. (2015). Ammonia emissions in tropical biomass burning regions: Comparison between satellite-derived emissions and bottom-up fire inventories. *Atmospheric Environment*, *121*, 42–54. https://doi.org/10.1016/j.atmosenv.2015.03.015

Wizenberg, T., Strong, K., Jones, D., Lutsch, E., Mahieu, E., Franco, B., & Clarisse, L. (2022). Replication data for: Exceptional wildfire enhancements of PAN, C_2H_4, CH_3OH, and HCOOH over the Canadian high Arctic during August 2017 [Dataset]. Borealis. https://doi.org/10.5683/SP3/6PBAHK

Yamanouchi, S., Strong, K., Lutsch, E., & Jones, D. B. (2020). Detection of HCOOH, CH_3OH, CO, HCN, and C_2H_6 in wildfire plumes transported over Toronto using ground-based FTIR measurements from 2002–2018. *Journal of Geophysical Research: Atmospheres*, *125*(16), e2019JD031924. https://doi.org/10.1029/2019jd031924

Yokelson, R. J., Crounse, J. D., DeCarlo, P. F., Karl, T., Urbanski, S., Atlas, E., et al. (2009). Emissions from biomass burning in the Yucatan. *Atmospheric Chemistry and Physics*, *9*(15), 5785–5812. https://doi.org/10.5194/acp-9-5785-2009

Yu, K., Keller, C. A., Jacob, D. J., Molod, A. M., Eastham, S. D., & Long, M. S. (2018). Errors and improvements in the use of archived meteorological data for chemical transport modeling: An analysis using GEOS-Chem V11-01 driven by GEOS-5 meteorology. *Geoscientific Model Development*, *11*(1), 305–319. https://doi.org/10.5194/gmd-11-305-2018

Yu, P., Toon, O. B., Bardeen, C. G., Zhu, Y., Rosenlof, K. H., Portmann, R. W., et al. (2019). Black carbon lofts wildfire smoke high into the stratosphere to form a persistent plume. *Science*, *365*(6453), 587–590. https://doi.org/10.1126/science.aax1748

Yu, S. (2000). Role of organic acids (formic, acetic, pyruvic and oxalic) in the formation of cloud condensation nuclei (CCN): A review. *Atmospheric Research*, *53*(4), 185–217. https://doi.org/10.1016/s0169-8095(00)00037-5

Yurganov, L. N. (1997). Seasonal cycles of carbon monoxide over the Arctic and Antarctic: Total columns versus surface data. *Atmospheric Research*, *44*(1–2), 223–230. https://doi.org/10.1016/s0169-8095(97)00003-3

Zander, R., Duchatelet, P., Mahieu, E., Demoulin, P., Roland, G., Servais, C., et al. (2010). Formic acid above the Jungfraujoch during 1985–2007: Observed variability, seasonality, but no long-term background evolution. *Atmospheric Chemistry and Physics*, *10*(20), 10047–10065. https://doi.org/10.5194/acp-10-10047-2010

Zhao, Y., Strong, K., Kondo, Y., Koike, M., Matsumi, Y., Irie, H., et al. (2002). Spectroscopic measurements of tropospheric CO, C_2H_6, C_2H_2, and HCN in northern Japan. *Journal of Geophysical Research*, *107*(D18), ACH2-1–ACH2-16. https://doi.org/10.1029/2001JD000748